iScience

CellPress
OPEN ACCESS

Review

Thermodynamic mechanisms governing icing: Key insights for designing passive anti-icing surfaces

Zhengzheng Xu,[1,4] Guoyong Wang,[1,4,*] Shuangxin Li,[1] Danqing Li,[1] Wenting Zhou,[2] Chuncheng Yang,[1] Huan Sun,[3] and Yan Liu[2,*]

[1]Key Laboratory of Automobile Materials, Department of Materials Science and Engineering, Jilin University, Changchun 130025, P.R. China
[2]Key Laboratory of Bionic Engineering (Ministry of Education), Jilin University, Changchun 130022, P.R. China
[3]Department of Cardiology, China-Japan Union Hospital of Jilin University, Changchun 130033, P.R. China
[4]These authors contributed equally
*Correspondence: materwanggy@jlu.edu.cn (G.W.), lyyw@jlu.edu.cn (Y.L.)
https://doi.org/10.1016/j.isci.2024.111668

SUMMARY

In winter, while the freezing of water can create breathtaking landscapes, it also poses significant operational challenges when ice accumulates on functional surfaces. Ice obstructs solar panels, impairs car windshield visibility, increases energy consumption in appliances due to insulation, and can cause structural failures or collapses due to weight and rigidity. To address these issues, various active de-icing methods are employed in cold regions. However, passive anti-icing solutions are gaining preference for their lower energy consumption, cost-effectiveness, and environmental benefits. While superhydrophobic surfaces delay ice formation, they do not fully resolve the problem. Understanding the interaction between surfaces and moisture—essential for ice formation—can inspire innovative anti-icing design principles. This review examines icing physics, identifies critical environmental factors affecting ice formation, evaluates icephobic surfaces, and discusses practical application challenges. We also outline promising design principles for passive anti-icing surfaces, emphasizing their broad applicability across diverse environments.

INTRODUCTION

Nature sustains life, yet it also poses significant challenges to survival and growth. Water, one of the nature's most essential resources, also exhibit a dual nature. On one hand, it is vital for life; on the other, it can be destructive if not managed properly.[1–3] Centuries ago, humans developed effective techniques to repel water, using natural oils and waxes to keep crops fresh and maintain body warmth.[4,5] Following Thomas Young and Gibbs' discoveries regarding solid-liquid interactions and surface energy,[6,7] Wenzel and Cassie-Baxter expanded on this by emphasizing the role of surface roughness in wettability.[8–10] This understanding has been crucial for the development of new water-repellent coatings.[11–14] In the 1990s, the combination of low-surface-energy polymers with micro- and nanoscale textured surfaces led to the creation of superhydrophobic surfaces (SHS), characterized by water contact angles exceeding 150° and contact angle hysteresis (CAH) below 5°.[15–17] The incorporation of microstructures with double re-entrant curvature and a low solid fraction enhanced surface repellence, even against low-surface-energy liquids such as methanol and glycerol.[18–20] SHSs have numerous applications in water-related fields, including self-cleaning (where rolling droplets remove dust),[21] reducing frictional drag on ship hulls,[22] improving buoyancy,[23] providing corrosion resistance,[24] enabling oil-water separation,[25,26] and creating stain-resistant textiles.[27] While human ingenuity in developing surfaces to repel water has grown increasingly sophisticated, these surfaces face significant challenges when applied to ice management.

Currently, more than half of the global population resides in areas with sub-zero temperatures. In 2008, sleet triggered widespread blackouts in southern China.[28,29] The weight of accumulated ice can collapse cables and even topple pylons. Ice accretion can also disrupt communication systems, block road and rail networks, and pose significant risks to aircraft flight safety.[30] On airplane wings, ice can severely alter the flight's dynamic characteristics. Ice accretion damages helicopter blades,[31] and adversely affects offshore oil platforms,[32] locks,[33] and dams.[34] Frost formation on refrigerators and heat exchangers can reduce heat transfer efficiency by as much as 50–75%.[35] On wind turbines, ice accretion significantly lowers aerodynamic efficiency and torque, leading to power losses of up to 50%.[36] Solar panels can become functionally useless when covered by just a few millimeters of snow.[37] The most widely used anti-icing and de-icing strategies today are active, but they are energy-intensive, inefficient, and environmentally unfriendly.[38–40] Mechanical de-icing of overhead cables can disrupt power supplies, potentially damage the cables, and pose safety risks to workers.[41,42] Using Joule heating, where current is passed through an object to prevent icing, is typically energy-consuming, costly, and can reduce

the lifespan of the equipment.[43] Chemical de-icing, commonly used in aviation to prevent ice buildup on planes, helicopters, runways, and on roads, is often inefficient, short-lived, and ecologically harmful due to its toxicity and corrosiveness.[44,45] Moreover, all of these methods necessitate continuous, active intervention by personnel.

Therefore, designing functional surfaces that can manage ice is just as intriguing as designing surfaces that repel water.[46–48] Currently, the fundamental requirement for such surfaces is the ability to prevent ice accumulation. These surfaces should either prevent the direct formation of ice or reduce the adhesion, making ice removal easier.[49–52] Despite the high demand, researchers are still uncertain about the specific surface characteristics that confer these anti-icing properties. Various laboratories have synthesized ice-phobic surfaces, including superhydrophilic, hydrophobic, superhydrophobic, and slippery surfaces, all of which have been thoroughly studied. Each of these surfaces demonstrates anti-icing potential under certain conditions. For instance, certain hydrophilic surfaces can lower the freezing point of water, which facilitates the sliding of ice due to the presence of an unfrozen water layer.[53] Slippery surfaces incorporating lubricating liquids can reduce ice adhesion to levels near the threshold (~5 kPa), where ice can self-remove via vibration or wind.[54–56] The momentum of impinging droplets, combined with the ultra-low adhesive force between liquid and superhydrophobic surfaces, shortens the contact time, even beyond the heterogeneous nucleation time of supercooled water.[57,58] Research on the anti-icing and de-icing performance of these surfaces has greatly advanced our understanding of icephobic materials. However, the icephobic properties of all current surfaces are challenged in extreme conditions, such as strong winds, sharp temperature drops, and sudden humidity surges caused by the collision of cold and warm air currents.[59,60] These surfaces also face challenges when transitioning between warm indoor conditions and freezing outdoor environments, particularly as warm surfaces cool during snowfall. In laboratory settings, an icing delay of over 3 h is generally considered a significant achievement.[61] However, cold nights often exceed this time frame, especially during the prolonged winters of high-latitude regions. Any failure in the water-repelling properties of ice-phobic surfaces can lead to the catastrophic loss of their de-icing capabilities.[62] The depletion of lubricants on slippery surfaces during de-icing further challenges their long-term durability.[63]

Recent advancements in the field have led to the development of superhydrophobic surfaces with enhanced stability and durability. For instance, surfaces with conical microstructures have been shown to exhibit superior Cassie-Baxter state stability compared to those with other micro/nanostructures.[64–66] These conical structures facilitate the expulsion of water and the spontaneous recovery of the Cassie-Baxter state after icing/melting cycles, ensuring long-term anti-icing performance. In addition to surface morphology, the use of advanced fabrication techniques, such as femtosecond laser processing, has further enhanced the properties of superhydrophobic surfaces.[67] This technology allows for precise control over the surface structures, resulting in surfaces with exceptional water repellency. Looking ahead, the design of functional surfaces for ice management will continue to evolve, with researchers focusing on optimizing surface characteristics to achieve even higher levels of anti-icing performance. This includes the development of surfaces with multifunctional properties, such as photo-electro-thermal effects, which can be utilized for all-day anti-icing/de-icing applications.[68,69] Similarly, another study described the use of femtosecond laser-structured black superhydrophobic cork for efficient solar-driven cleanup of crude oil.[70] This material exhibited superior hydrophobicity and photothermal conversion efficiency, making it suitable for marine oil spill remediation. In summary, advancements in superhydrophobic surfaces and their applications in anti-icing and oil spill cleanup demonstrate the potential of these technologies in addressing real-world challenges. By mimicking nature and leveraging modern fabrication techniques, researchers continue to push the boundaries of material science, striving for more sustainable and efficient solutions. This review provides an overview of recent advancements in anti-frosting and de-icing surfaces, setting the stage for further in-depth research. Scheme 1 illustrates the core elements of this review, covering the thermodynamic mechanisms and kinetic pathways of the icing process. It also evaluates current anti-frosting strategies, passive de-icing methods, and their underlying mechanisms. Finally, we offer prospective suggestions for the future design of icephobic surfaces.

Thermodynamic driving force for water condensation and freezing

Severe ice accretion on smart surfaces typically originates from the freezing of condensed droplets, such as frost, or fallen droplets such as sleet and freezing rain. Solid precipitation, including snowflakes, hailstones, and graupel, can also lead to significant ice accumulation on smart surfaces in a short period of time. In the absence of melting or freezing, the adhesion stress of this ice accumulation on smart surfaces is typically quite low. Such ice can usually be removed by strong winds, gravity, or simple cleaning, restoring the functionality of the surface.[73,74] However, when water droplets, condensation, or frost freeze on smart surfaces, ice accretion becomes a major issue. The ice-covered surface replaces the original smart surface, and the advanced properties of the smart surface, often developed through sophisticated technology, are lost. The new surface property becomes rough and hydrophilic ice, which acts as a humidity sink due to the much lower vapor pressure of ice compared to water in cryogenic environments.[75–77] Therefore, it is common to observe ice growth in cryogenic and humid conditions. These surfaces can lead to catastrophic outcomes when exposed to freezing rain. To clarify the conditions for condensation and freezing, we will first examine the water phase diagram, as shown in Figure 1A[71] The phase diagram outlines the regions of pressure and temperature where the various phases of water (gas, liquid, solid) are thermodynamically stable. At 1 atm (101.325 kPa), the temperature of 0°C (273.16 K) lies on the liquid-phase boundary, which separates water into the solid phase (ice) and liquid phase (water), as indicated by point A on line α in Figure 1A. Any temperature deviation at 1 atm will result in a shift along the line α,

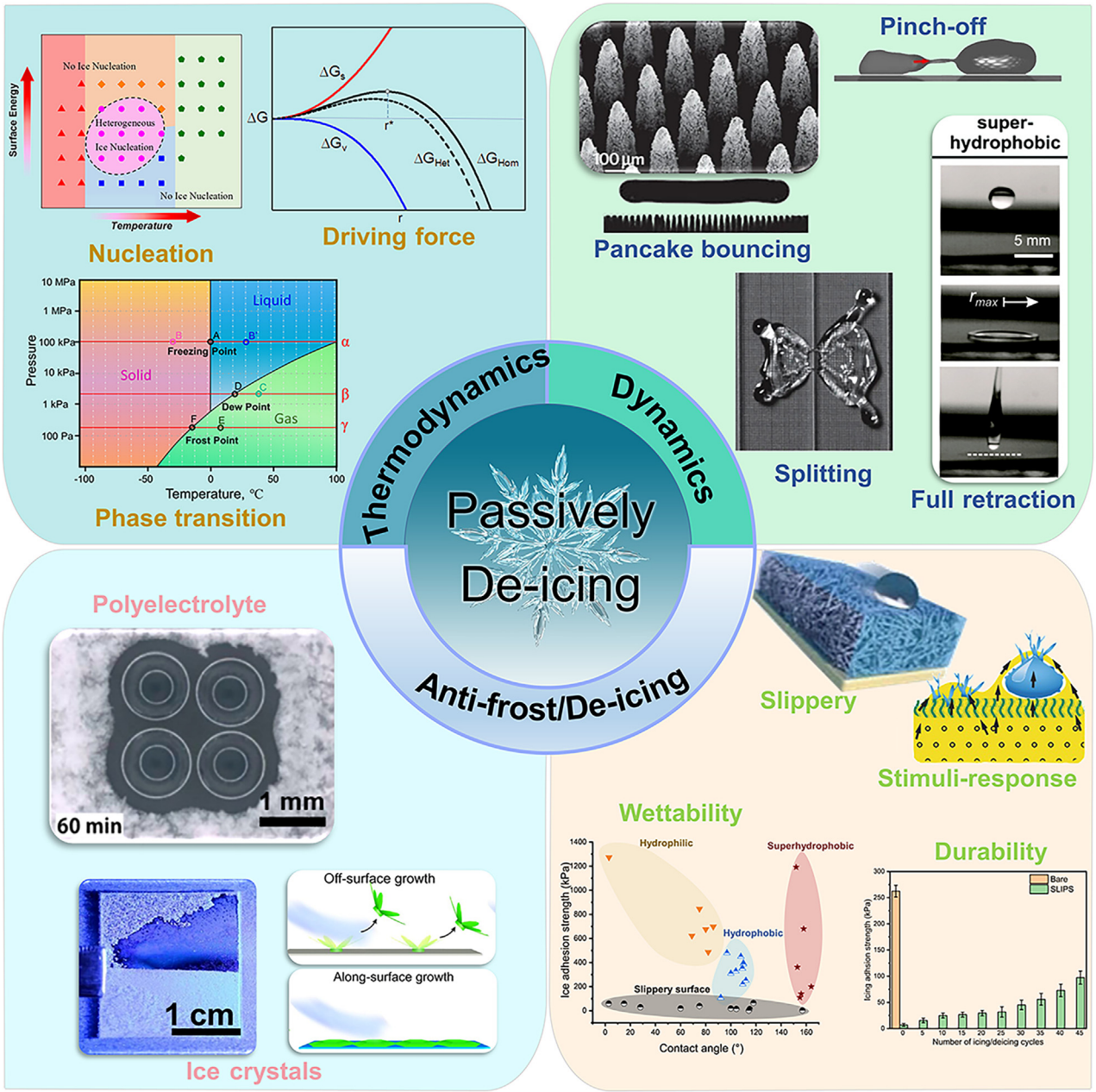

Scheme 1. Schematic illustration of passively de-icing strategies

moving away from the boundary. The point will then fall either in the solid-phase zone or the liquid phase zone, as represented by the point B or B′ along line α in Figure 1A. If the water is not in the corresponding phase, it will exhibit a thermodynamic tendency to undergo phase transitions, either from liquid to solid or vice versa. Special attention should be given to the triple point, occurring at 273.16 K and 611 Pa. The solid-liquid boundary near the triple point remains nearly vertical until pressures exceed 10 MPa. Even without temperature change, phase transitions continue under pressure variations, resulting in volume changes in water and ice, with heat transfer occurring within the system.

The horizontal line α in Figure 1A illustrates the transition pathway between the solid and liquid phases at 1 atm. However, phase transitions between vapor-liquid, and vapor-solid can occur anywhere along the boundary of the vapor region. In the phase diagram, pressure represents the vapor partial pressure under atmospheric conditions, which can theoretically vary from 0 Pa to 1 atm. Under normal atmospheric conditions, air humidity rarely reaches 100%. Therefore, vapor pressure is expected to remain below the vapor-phase boundary and lower than 1 atm, as indicated by the point C on line β (representing typical summer conditions) or point E on line γ (representing

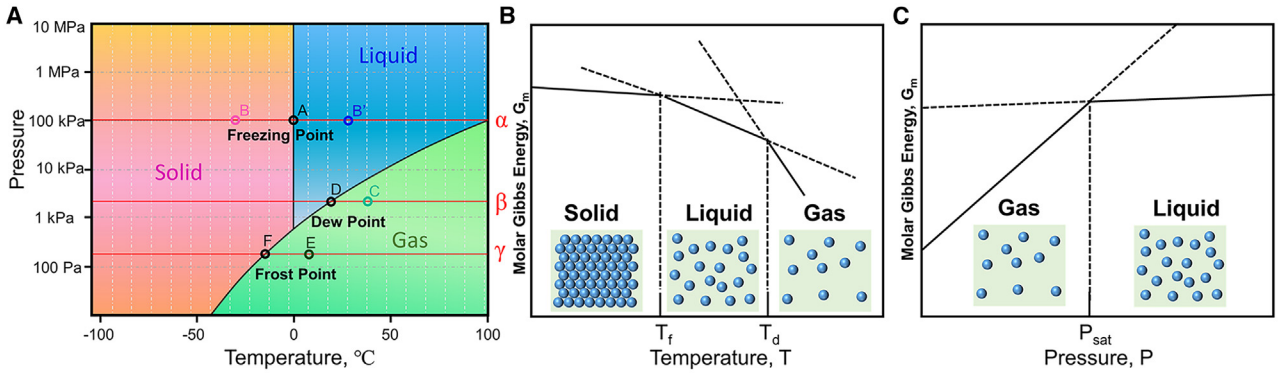

Figure 1. The phase diagram of water and its thermodynamic principles

(A) The experimental phase diagram for water showing the different thermodynamic stable phases.[71]

(B) The dependence of the chemical potential of the solid, liquid, and gas phases on the temperature.[72] The phase with the lowest chemical potential at a specified temperature is the most stable one at that temperature. The transition temperatures (T_f and T_d), are the temperatures at which the chemical potentials of the both phases are equal.

(C) The dependence of the chemical potential of the liquid and gas phase on the pressure.

typical winter conditions). When temperatures drop suddenly during nightfall or a cold front, the process can be considered isobaric, as the vapor partial pressure and the mole fraction of water vapor in the air at standard atmospheric pressure remain nearly constant. The state of water shifts along the line β to the liquid-phase zone or along line γ to the solid-phase zone, depending on vapor pressure. The intersection with the gas/liquid boundary (known as the dew point) or the gas/solid boundary (known as the frost point) occurs. At this stage, air humidity exceeds 100% and vapor pressure rises above the vapor-phase boundary, creating a thermodynamic tendency for condensation or freezing. While it may appear that temperature or pressure drives water's phase change, the true driving force is the molar Gibbs energy: a key thermodynamics property. Its decline represents the spontaneous direction of the process, in accordance with the second law of thermodynamics.[78] In the following section, we will explore the relationship between temperature, pressure, and molar Gibbs energy.

Similar to Figure 1B, in meteorology, sudden temperature drops are often accompanied by the intrusion of cold air, which can cause water vapor to rapidly condense into dew or frost. This process not only affects the physical state of the ground and object surfaces but also has implications for industries such as agriculture, transportation, and construction. For example, icy roads can impact traffic safety, and ice accumulation on building surfaces can lead to structural damage. Understanding the thermodynamic principles behind these phase transitions can help in developing effective anti-icing technologies and strategies to mitigate the negative impacts of adverse weather conditions. Additionally, by studying the changes in molar Gibbs free energy under different conditions, scientists can better predict and control the phase transitions of water, providing a scientific basis for weather forecasting and disaster prevention.

Weather changes are more closely aligned with an isobaric process. Therefore, the temperature dependence of the molar Gibbs energy in an isobaric process is expressed in terms of the system entropy by the following equation[79]:

$$\left(\frac{\partial G_m}{\partial T}\right)_P = -S_m \qquad \text{(Equation 1)}$$

Where G_m is molar Gibbs free energy, T is temperature; P is pressure; S_m is molar entropy. For all substances, $S_m > 0$. So the slope of G_m against T is negative, as shown in Figure 1B. This means that under isobaric conditions, as the temperature increases, the Gibbs free energy of the substance decreases, thereby affecting the phase transition process.[80,81] Because $S_m(g) > S_m(l) > S_m(s)$, the slope for gas is steepest and the slope for solid is smoothest. The successively steeper negative slope of molar Gibbs free energy of the three phase results in $G_m(s)$ is lowest as the temperature is below T_f, $G_m(l)$ is lowest as the temperature is between T_f and T_d, $G_m(g)$ is lowest as the temperature is above T_d. Thus, as the temperature increases from below T_f to above T_d, the solid melts initially and the liquid then vaporizes finally.[82] Similar to that, the vapor pressure dependence of the molar Gibbs energy in the isothermal process is expressed in terms of the volume of the system by the following equation[83]:

$$\left(\frac{\partial G_m}{\partial p}\right)_T = V_m \qquad \text{(Equation 2)}$$

Here V_m is the molar volume. For $V_m(g) > V_m(l)$, $G_m(g)$ is lower as the pressure is below the equilibrium vapor pressure while $G_m(g)$ is higher as the pressure is above the equilibrium vapor pressure (Figure 1C). An isothermal process refers to a process where the temperature inside the system or between the system and its surroundings remains constant with no heat exchange. In atmospheric science, isothermal processes can affect the stability and temperature distribution of the atmosphere. For example, when the atmosphere is in an isothermal state, the temperature gradient is small, which can lead to stable atmospheric stratification, thereby influencing convective activity and cloud formation. Under isothermal conditions, the

likelihood of water vapor condensing into clouds in the atmosphere is lower because there is an insufficient temperature gradient to drive upward air currents.[84] It is noteworthy that such isothermal processes are not common in meteorology.

By gaining a deeper understanding of the phase transitions of water and their thermodynamic principles, we can better predict and manage ice accumulation caused by sudden temperature drops. This knowledge not only enhances the accuracy of weather forecasts but also provides scientific support for the development of anti-icing technologies and strategies, thereby reducing the negative impacts of adverse weather conditions on society and the economy. The phase diagram and associated data in Figure 1 provide important references, helping us to more accurately understand and predict these complex meteorological phenomena.

Thermodynamic barriers for nucleation

However, to complete the temperature change and phase transition described above, water must undergo a series of steps. First, it must undergo a heat transfer process to lower its temperature due to its high specific heat capacity (liquid water: 4.2 J/(g·K); solid water: 2.1 J/(g·K)).[85] During the phase transition process, another heat transfer process occurs due to the relatively high standard enthalpies of fusion (6.008 kJ/mol at 273.15 K) and vaporization (44.016 kJ/mol at 298 K).[86] A 1 mL raindrop, as it freezes into ice at 273.15 K from either gas or water at 298 K, must release 2.88 kJ or 0.44 kJ of heat to the surrounding air.[87] Assuming the temperature gradient is confined to a 5 cm layer of air around the droplet, and the temperature difference remains at 5 K, it would take 38256 s or 5812 s to complete the phase transition, given the air's thermal conductivity is 0.024 W/(m·K).[88] In theory, this provides ample time to remove the drop from the surface before it freezes. This is a fundamental reason why superhydrophobic surfaces have garnered significant attention for anti-icing applications.[89] On superhydrophobic surfaces, the falling raindrops typically bounce back and fall away under gravity within 1 s. However, real-world scenarios tend to be more challenging than this theoretical prediction. As raindrop size decreases, the specific surface area increases, which in turn raises the rate of heat dissipation.[90] More critically, the thermal conductivity of most solid materials is over 40 times higher than that of air. If metals such as copper, with a thermal conductivity of 401 W/(m·K), are used to fabricate superhydrophobic surfaces,[91,92] the heat dispersal time shortens dramatically down 1530 s or even 232 s, even if the contact area is just one-thousandth of the droplet's surface. Additionally, raindrops may encounter strong winds, which can accelerate vaporization. Because of water's high vaporization enthalpy, even a small amount of vaporization removes significant heat, causing a sharp temperature drop. In such cases, the time window becomes even narrower. It is also notable that the enthalpy of water fusion is sufficient to theoretically heat an equivalent amount of water by 75 K.[93–95] Even when supercooled water reaches temperatures as low as 233 K, it must still transfer excess heat to fully freeze. Freezing rain, too, requires a heat transfer step before solidifying. The release of the enthalpy of fusion raises the temperature of the ice formed from supercooled droplets above that of its surrounding environment.[96] Thus, there is always a window of time to remove water before it freezes.

When temperatures fall below 0°C, the water-to-ice phase transition does not begin immediately. Further cooling or a period of time is required for water to accumulate enough Gibbs free energy to form an ice nucleus.[97] The formation of a new phase inevitably creates an interface between the new phase and the parent phase. For a phase transition to occur, the parent phase requires a certain level of supercooling and/or supersaturation, as shown in Figures 1B and 1C. The molar Gibbs free energy difference between the parent and the new phases must exceed the interfacial energy. Under these conditions, the phase transition process results in a continuous reduction of Gibbs free energy. Classical nucleation theory assumes that the new phase nucleus is spherical, with a specific chemical potential and surface free energy, to minimize uncertainties related to embryo shape and size.[98,99]

According to this theory, the total change in the Gibbs free energy during a phase transition is governed by the increase in newly generated surface energy and the decrease in Gibbs free energy per unit volume from the newly formed phase, as described by the following equation[103]:

$$\Delta G = \textit{surface term} + \textit{volume term} = 4\pi r^2 \gamma_{SL} - \frac{4}{3}\pi r^3 \Delta G_V \quad \text{(Equation 3)}$$

Where ΔG represents the change in Gibbs free energy (J), r is the radius of the nucleus (m), γ_{AB} is the interfacial energy between the new solid phase S and the parent liquid phase L (J/m^2), and ΔG_V is the Gibbs free energy change per unit volume (J/m^3). At a given temperature, the Gibbs free energy change reaches a maximum,[98] as shown in the following equation:

$$\Delta G* = \frac{16\pi\gamma_{SL}^3}{3\Delta G_V^2} \quad \text{(Equation 4)}$$

for a critical radius:

$$r^* = -\frac{2\gamma_{SL}}{\Delta G_V} \quad \text{(Equation 5)}$$

Beyond this critical radius, any further increase in r will cause ΔG to decrease, as illustrated in Figure 2A. Embryo shapes other than spherical are possible, and the results must be adjusted by a shape factor, which is typically greater than one. The height of the thermodynamic barrier and the critical radius for nucleation vary and depend significantly on the ΔG_V. The value of ΔG_V is related to the degree of supercooling, as shown in the following equation:

$$\Delta G_V = -\Delta S_V \Delta T \quad \text{(Equation 6)}$$

Where ΔS_V represents the average entropy of fusion over the supercooling range ΔT. Increasing the degree of supercooling can significantly reduce both the energy barrier and the critical radius, though the energy barrier will never be completely eliminated. This energy barrier can only be overcome through thermal

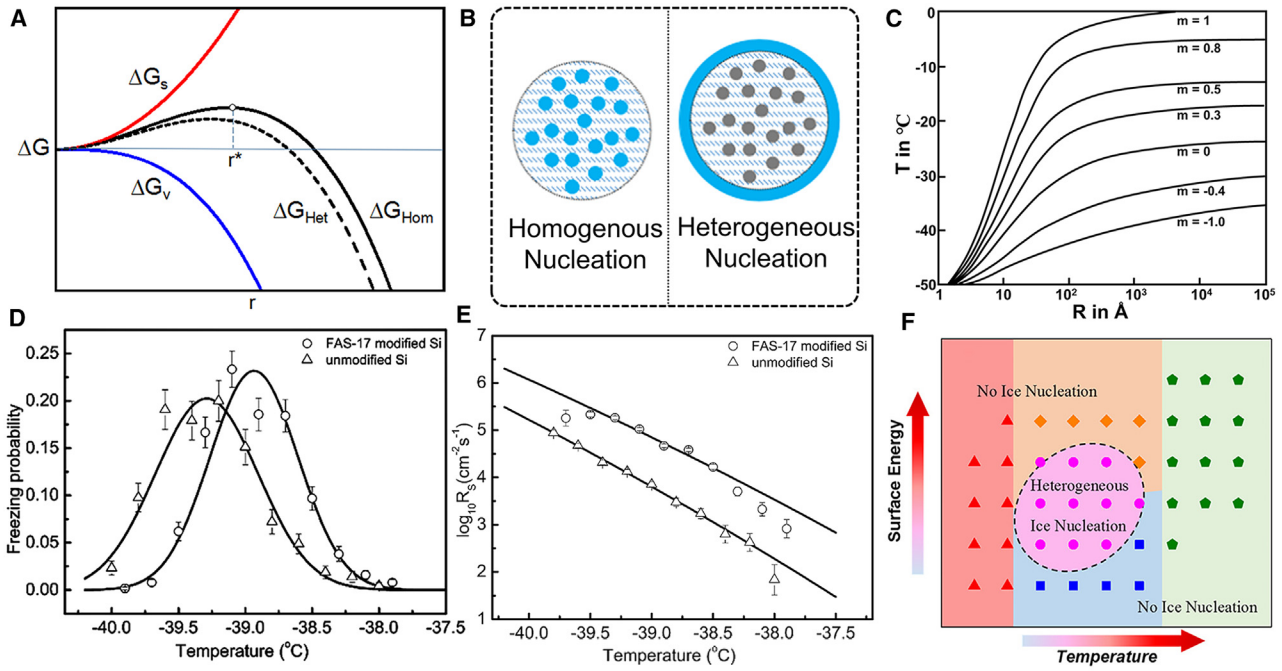

Figure 2. Gibbs free energy changes and nucleation theory during phase transitions

(A) Relationship between the Gibbs free energy.

(B) Schematic diagram of homogeneous nucleation and heterogeneous nucleation.

(C) Temperature T below which a particle of radius r and surface parameter $m = \frac{\gamma_{PL}-\gamma_{SP}}{\gamma_{SL}}$ will nucleate an ice crystal by freezing in less than 1 s.[100]

(D) Freezing probability distribution as a function of temperature on the unmodified hydrophilic silicon wafer surface.

(E) Surface ice nucleation rate as a function of temperature. (D) and (E) produced with permission[101] from the *American Chemical Society*.

(F) Computer simulations show that heterogeneous nucleation can only occur on a surface with special surface energy in a special temperature range. Produced with permission[102] from the *American Chemical Society*.

fluctuations. Therefore, there is no exact temperature at which an embryo forms and freezing begins. This theoretical deduction is strongly supported by extensive experimental evidence, as the homogeneous nucleation temperatures measured by different researchers using various methods exhibit wide variation.[96] This energy barrier can be overcome be more easily overcome if the ice embryo forms on a foreign particle's surface, which can act as a nucleation site when introduced into a solution. This process is known as heterogeneous nucleation[104] (Figure 2B). For a foreign particle of arbitrary size and shape, a simplified equation for heterogeneous nucleation can be written as follows, where the subscript *P* refers to the particle[105]:

$$\Delta G = V_S \Delta G_V + \gamma_{SL} A_{SL} + (\gamma_{SP} - \gamma_{PL}) A_{SP} \quad \text{(Equation 7)}$$

Assuming the foreign particle is spherical, and the ice embryo grows on its surface with a negligible initial thickness, the free energy involved in heterogeneous nucleation can be simplified as follows:

$$\Delta G = 4\pi r^2 \gamma_{SL} + 4\pi r^2 (\gamma_{SP} - \gamma_{PL}) + \frac{4}{3}\pi r^3 \Delta G_V \quad \text{(Equation 8)}$$

By comparing Equation 3 and Equation 8, it becomes clear that a foreign surface aids in overcoming the energy barrier only when $(\gamma_{SP} - \gamma_{PL}) < 0$, and the particle radius exceeds the theoretical radius r^*. Currently, there are few effective methods to measure interfacial energy during heterogeneous nucleation. Therefore, Equation 7 cannot be used for material verification but serves as a general guide for material selection. For example, materials that introduce elastic strains across the interface due to high lattice mismatch are typically not suitable for heterogeneous nucleation, as they increase the free energy according to Equation 7.

The energy barrier created by a new phase interface makes the water-to-ice phase transition more challenging.[106] Supercooling allows energy to accumulate for the subsequent phase transition.[107,108] The presence of heterogeneous surfaces can effectively lower the energy barrier. The phase transition occurs when the energy from supercooling and thermal fluctuations exceeds the energy barrier. Both the energy from supercooling and the energy barrier are fixed values at certain temperatures and circumstances.[109] However, thermal fluctuations cause the freezing temperature to be variable. As shown in Figure 2C, the theoretically calculated freezing temperature is constant for heterogeneous cores with different sizes, whereas experimental measurements show freezing temperatures spread over a wide range, as shown in Figure 2D.[101] The presence of heterogeneous surfaces does not always promote nucleation. If the heterogeneous core size is smaller than the critical r^* or if the interfacial energy between the particle and ice is very high, heterogeneous

nucleation becomes more difficult than homogeneous nucleation, as shown in Figure 2C.[100] In experiments, a higher nucleation rate was observed on superhydrophobic surfaces compared to wettable surfaces, as shown in Figure 2E.[101] According to computer simulations, even when a surface is fully wetted by water, heterogeneous ice nucleation only occurs on surfaces with specific surface energies within a particular temperature range, as shown in Figure 2F.[102]

Timely repelling of water droplets for effective anti-icing

As previously discussed, the condensation and freezing processes are spontaneous and inevitable under suitable temperature and pressure conditions. However, the timing and position of phase transitions can be influenced by homogeneous or heterogeneous nucleation within the region. Therefore, it is both unnecessary and unlikely for passive anti-icing smart surfaces to completely inhibit the condensation or freezing of water or vapor under harsh conditions. Instead, passive anti-icing surfaces aim to prevent phase transitions from occurring directly on the surface or confine them to designated areas, thereby reducing the contact area and lowering ice adhesion strength to levels that make de-icing easier. Fallen water droplets must leave the surface as quickly as possible, either by bouncing or sliding off,[110] before freezing occurs. In other words, the anti-icing effectiveness of a surface depends on the competition between its ability to repel water and its tendency to trigger freezing. If water repulsion dominates, the surface remains clean. Otherwise, the surface becomes covered with accumulated ice. Thus, surfaces exhibiting at least one of the three key factors—short repelling time, extended incubation period before freezing, or optimized freezing location—can function as effective anti-icing surfaces. In the following sections, we will summarize the surface parameters that influence these three critical factors.

Minimizing droplet bouncing time for enhanced anti-icing

When a water droplet falls onto a solid surface, its kinetic energy, derived from its velocity, causes the drop to flatten from its initial spherical shape into a pancake shape. During this process, although surface tension remains constant, the conversion of kinetic energy into surface energy increases sharply as the droplet's surface area expands. Whether the surface energy of the droplet can be converted back into kinetic energy depends largely on the strength of the interaction between the droplet and the solid surface. If the molecular interactions are weak, as on superhydrophobic surfaces[111] or when an air cushion forms between the droplet and the surface, the droplet's surface tension works to minimize its surface area. In this case, most of the initial kinetic energy is restored, except for losses due to internal dissipation, allowing the droplet to bounce off the surface. However, if the molecular interactions are strong, the droplet remains flattened in its pancake shape and adheres to the surface.[112] Homogeneous nucleation temperature was first measured on hydrophobic surfaces, where the extremely low contact area rendered heterogeneous nucleation negligible.[113] By combining ultralow surface energy with multimodal roughness, superhydrophobic surfaces achieve water contact angles above 150° and exhibit very low contact angle hysteresis ($\leq 5°$) due to a stable air cushion beneath the droplet. This provides direct experimental evidence of the ultralow contact area.[114] As a result, droplets on superhydrophobic surfaces behave like free-flowing droplets without significant heterogeneous interference. Additionally, the ultralow contact area results in minimal heat transfer and greater mobility for the droplets. These properties greatly increase the likelihood that droplets will leave the surface before freezing. That is why superhydrophobic surfaces are often regarded as promising candidates for passive de-icing applications.[115]

Mishchenko et al. conducted a comprehensive comparison of the impact behavior of droplets at temperatures ranging from +60 to −5°C on tilted and flat hydrophilic, hydrophobic, and superhydrophobic substrates, with surface temperatures ranging from +20 to −30°C,[116] as shown in Figure 3A. Liquid precipitation that leads to ice accretion, such as freezing rain, frozen dew, glaze, flash freezes, and black ice, takes seconds to hours to freeze in sequence.[119,120] Freezing rain provides the shortest time window before freezing, making it the most difficult to manage. This experiment simulated the freezing rain process by using supercooled water droplets. Due to the excellent water-repelling ability and low heat transfer of superhydrophobic substrates, impacting water droplets have sufficient energy and time to retract and slip off, while droplets freeze on another type of substrate surfaces. Under the same conditions, the time it takes for droplets to freeze on a superhydrophobic surface (droplet 2) is significantly longer than on a flat hydrophobic surface (droplet 1) and a partially wetting surface (droplet 3), as shown in Figure 3B. As a result, the superhydrophobic surface prevented ice accretion until the surface temperature dropped to −25°C.[110] This research highlights the great potential of superhydrophobic surfaces for passive anti-icing applications. It is important to note that −25°C is much colder than the typical ground temperature during freezing rain. Ground temperature usually does not fall below −10°C during freezing rain, as lower temperatures would result in solid precipitation, such as sleet, graupel, and snow.[121,122] Furthermore, the contact time of falling water droplets on a superhydrophobic surface remains nearly constant within 14 ms,[117,118,123] regardless of impacting speed and the *We* number, as shown in Figures 3C and 3D. This consistent contact time is a crucial characteristic of superhydrophobic surfaces, as it implies that these surfaces can effectively repel water under a wide range of conditions, making them ideal for applications where rapid water shedding is essential to prevent ice formation and maintain surface performance.

Though the underlying mechanism is not fully understood, it is believed that the stretching and retraction processes of falling droplets on superhydrophobic surfaces occur within a constant time, regardless of the maximum pancake size.[126] Ignoring the heat transfer process and the incubation time required for thermal fluctuation to trigger nucleation, the ice nucleus growth rate in supercooled water droplets at −15°C is only 0.1 mm/ms[124] after homogeneous nucleation in unsaturated gas flow, as shown in Figure 4A[98] The droplet in this image has a volume of 5 μL and a diameter of about 1.5 mm, which is typical for summer raindrops, as shown in Figure 4B. Thus, it takes over 15 to 18 ms for the droplet to fully freeze after nucleation, which exceeds the contact time of a droplet bouncing off on a

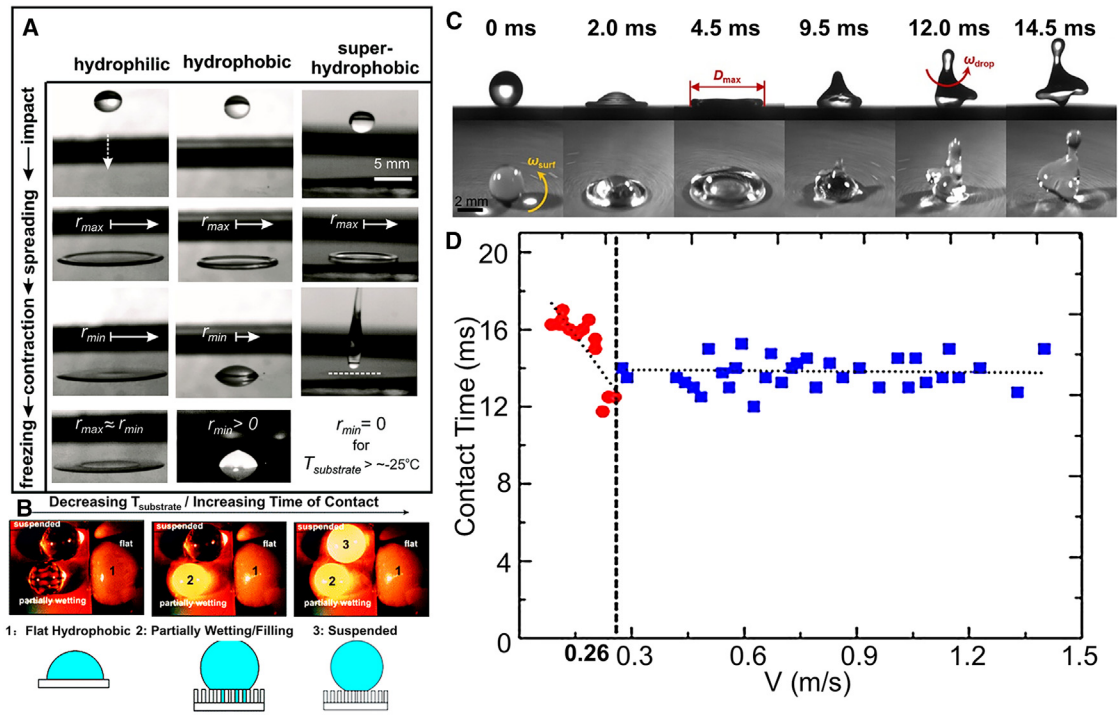

Figure 3. Contact time of dynamic water droplets on supercooled surfaces

(A) Sequential images of the dynamic behavior of ~15 μL droplets impacting cooled ($T_{substrate}$ < 0°C) horizontal surfaces from a 10 cm height.

(B) The temperature of the substrate was gradually decreased from 0 to −20 °C at a rate of −5°C/min (A) and (B) produced with permission[117] from the *American Chemical Society*.

(C) Dynamics of droplet impact on superhydrophbic surface with high-speed of rotating surface of $\omega = 628\,rad/s$. Produced with permission[117] from the *American Chemical Society*.

(D) The statistics contact time of droplets impacting on lotus leaf as a function on impacting velocity. Produced with permission[118] from *Elsevier B.V. All rights reserved*.

superhydrophobic surface. For heterogeneous nucleation, the freezing time doubles due to the poor thermal conductivity of ice between the water and the substrate, as shown in the second line of Figure 4A. As demonstrated in subsequent experiments, if the droplet's rolling velocity is high enough, it can even partially detach from existing ice crystals on the surface, provided the departing time is under 18 ms as shown in Figure 4C [117] and Figure 4D.[118] Thus, the 14 ms contacting time for bouncing droplets on superhydrophobic surfaces is sufficiently short to ensure that droplets can depart, at least partially, without forming ice on the surface. Recent research has further reduced the contact time to half or even one-quarter, reinforcing the potential for fallen water droplets to bounce off the surface before freezing.[127]

Yahua Liu et al.[126] reported that on a superhydrophobic copper surface patterned with a square lattice of tapered posts, a falling droplet with *We* more than 12 can bounce off within 3.4 ms (Figure 5A). The droplet does not need to complete the conversion of surface energy to kinetic energy. During the droplet descent and diffusion to the surface, it can acquire the capillary energy stored in the permeating liquid and thus get enough kinetic energy to bounce off. This kind of bouncing is called pancake bouncing, because the droplets still remain pancake shapes after they depart from the surface. This pancake bounce allows a 4-fold reduction in contact time compared to the conventional complete rebound.[131] Then, subsequent research indicates that the pancake bouncing occurs on across a wide range of superhydrophobic textures, including conical array (Figure 5B),[128] ridge surfaces (Figure 5C),[129] and large-area pillar arrays (Figure 5D),[130] though the contact time varies a little. This research simply opens another avenue to reduce the contact time of impacting droplets on a surface from the substrate perspective. Then, other research has investigated the pancake-bouncing behavior of water droplets on spherical surfaces and highly elastic substrates and achieved good progress.[132–136] Considering the actual size of raindrops and the growth rate of ice cores in supercooled water, pancake bouncing still offers the potential to remove the drops off the surface even if there are ice crystals on the surface, triggering the freezing of the supercooled water droplets. The findings highlight the potential of pancake bouncing as an effective mechanism for minimizing droplet contact time and preventing icing. Future research should focus on further exploring and optimizing this phenomenon across various materials and conditions to enhance practical applications in anti-icing technologies.

In addition to pancake bouncing, it is widely observed that droplet scattering significantly reduces contacting time.[137] As shown in Figure 6B, the full stretch and retraction of the impacting droplet are visible on superhydrophobic surfaces, compared

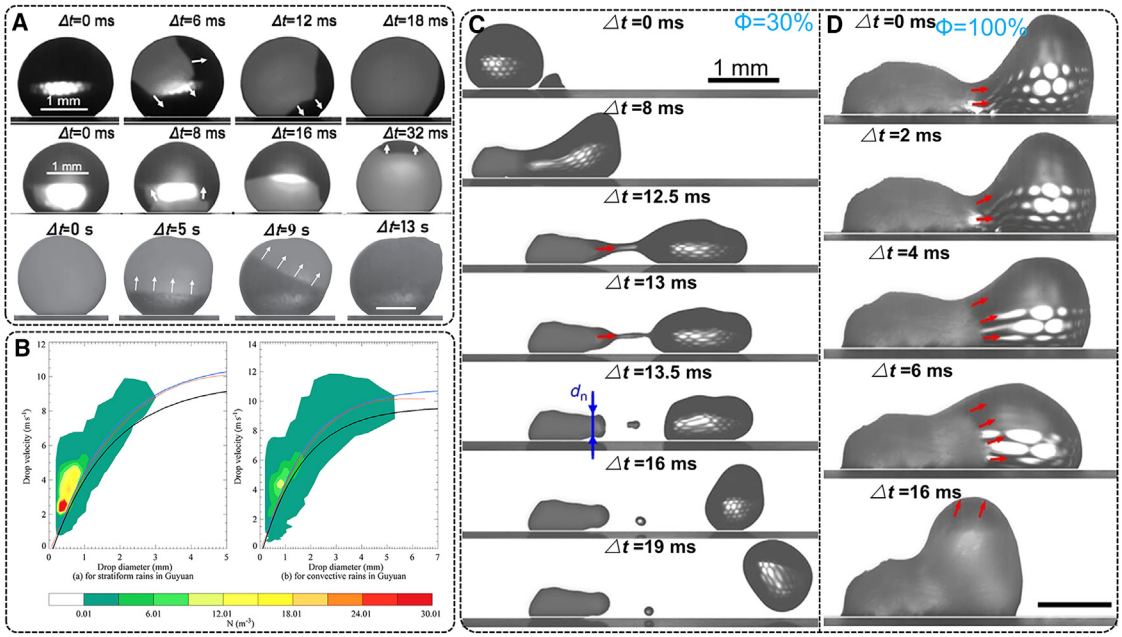

Figure 4. Raindrop diameter and supercooled sessile droplets under shear

(A) Origin of homogeneous nucleation at the gas–liquid interface followed by ice front propagation in a supercooled sessile droplet (top row), origin of heterogeneous nucleation at the liquid–solid interface followed by ice front propagation in a supercooled sessile droplet (bottom row).[124]

(B) Number concentration distribution (colors) as a function of the drop diameter and raindrop fall velocity for the stratiform rains and convective rains. Produced with permission[125] from the *American Meteorological Society*.

(C and D) Humidity dependent pinch-off and stickiness of supercooled droplets on superhydrophobic surfaces after encountering an ice cluster with dry surface (left, Φ = 30%) (C) and wet surface (right, Φ = 100%) (D). (A), (C), and (D) Produced with permission[124] from *Nature*.

to the partial stretch observed on the hydrophilic surface (Figure 6A) at low impact velocity. At high impact velocities, the droplet scatters into fragments, as illustrated in Figure 6C and Figure 6D. The scattering divides the pancake-shaped droplet into numerous fragments, creating multiple retraction centers. Assuming the contact angle at the edge of these fragments is the same as that of the whole droplet, the retraction velocity should be similar. However, because the distance from the edge to the retraction center is reduced, the total energy conversion time also decreases. Denis & David comprehensively investigated the contact time of an integral bouncing drop on a superhydrophobic surface.[131] They found that the contact time depends on the droplet radius R, liquid density ρ and surface tension γ, as described by the following equation:

$$\tau \approx \left(\rho R^3 / \gamma\right)^{\frac{1}{2}} \qquad \text{(Equation 9)}$$

This equation shows that reducing the droplet diameter can effectively shorten the contact time. The scatter of a big drop with a high Weber factor just leads to tens of droplets with a smaller diameter, which will shorten the contact time. For the droplets with a relatively low Weber number, an appropriately textured superhydrophobic surface can also cause the droplets to split. As shown in Figures 6E and 6F, periodically arranged macroscale ridges (~100 μm) on a superhydrophobic surface can split a falling droplet in half, similar to a razor blade.[90] This reduced the corresponding contact time by 37% to 7.8 ms. In addition to surface texture, a carefully designed surface energy distribution can also split water droplets into smaller fragments.[138]

Minimizing droplet sliding time: Balancing sliding speed and surface length

For droplets to avoid falling back onto the surface after the first bounce, the surface must be sufficiently inclined and small. Otherwise, the droplets may fall back onto the surface. After the initial bounce, the droplet's velocity is significantly reduced due to energy dissipation, and it may not bounce again.[140–142] In addition to the kinetic energy of the falling droplets, gravity provides a reliable force to help repel the droplets from the surface. As illustrated in Figure 7A, when the surface is sloped, one component of gravity pushes the droplet forward along the slope (parallel force F_P), while another component presses the droplet against the surface (perpendicular force F_n). If the parallel force exceeds the friction force (F_f), the droplet will slide down the slope. The droplet's velocity and acceleration at any given position can be determined by Newton's Second Law of Motion for a slope with angle α, as shown in Figure 7A, using the following equation:

$$v = v_0 + at = v_0 + (F_p - F_f)t / m \qquad \text{(Equation 10)}$$

Where v is the velocity, v_0 is the initial velocity, a is the acceleration due to gravity, m is the mass of the droplet, and t is the time.

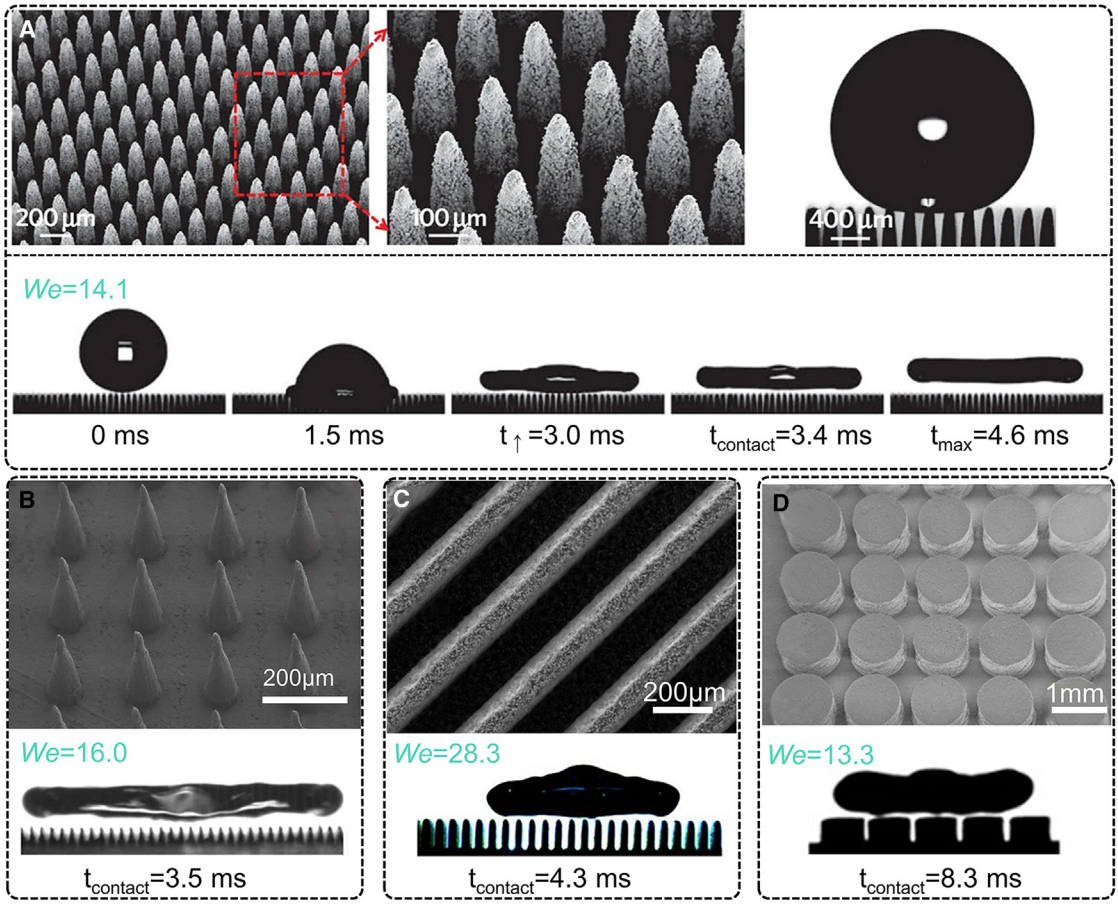

Figure 5. Pancake bouncing of droplets on superhydrophobic surfaces

(A) SEM image of copper surface with a lattice of tapered posts, exhibiting a contact angle of over 165°, showing snapshots with a droplet impacting on the surface at *We* = 14.1, the contacting time of the droplet was 3.4 ms. Produced with permission[126] from *Nature.*

(B) SEM image of PMDS with the conical array, showing the contact time of droplet 3.5 ms at *We* = 16. Produced with permission[128] from the *American Chemical Society*.

(C) SEM image of the copper surface with ridge structure with a droplet impacting on the surface at *We* = 28.3, and the contacting time of the droplet was 4.3 ms. Produced with permission[129] from the *American Chemical Society*.

(D) SEM image of PDMS with the pillar arrays, showing a snapshots with a droplet impacting on the surface at *We* = 13.3, the contacting time of the droplet was 8.3 ms. Produced with permission[130] from the *American Chemical Society*.

The F_f acting on a sliding droplet on a slope has been extensively studied, primarily characterized by dynamic contact angles, including advancing and receding contact angles. Although measurements vary slightly, as shown in Figure 7B through Figure 7D, they consistently show similar contact angle hysteresis. This value is crucial, as it allows the F_f of the droplet to be calculated using the following equation, assuming a circular contact region[143]:

$$F_f = \frac{24^{\pi^3}}{} \gamma D(\cos\theta_r - \cos\theta_a) \quad \text{(Equation 11)}$$

Where D is the diameter of the contact region and γ is the surface tension. However, as surfaces become increasingly slippery, the advancing and receding contact angles converge, and quantifying slipperiness through contact angle measurements becomes limited by the accuracy of image analysis.[143] The F_f can also be precisely measured using a high-speed camera. As shown in Figure 7E, the distance traveled by the sliding droplet is recorded over time by a high-speed camera. The resulting curve is fitted using the following equation as it follows Newton's Second Law of Motion:

$$L = \frac{1}{2}at^2 + v_0 t \quad \text{(Equation 12)}$$

After fitting, the acceleration is calculated as $a = (F_P - F_f)/m$. Since the droplet's mass is known for a fixed diameter droplet, the friction force can be easily calculated using these equations. This method is concise, and additional important parameters can also be derived from the data. For example, by differentiating the data, the velocity of the droplet as a function of distance can be obtained as shown in Figure 7F. From the

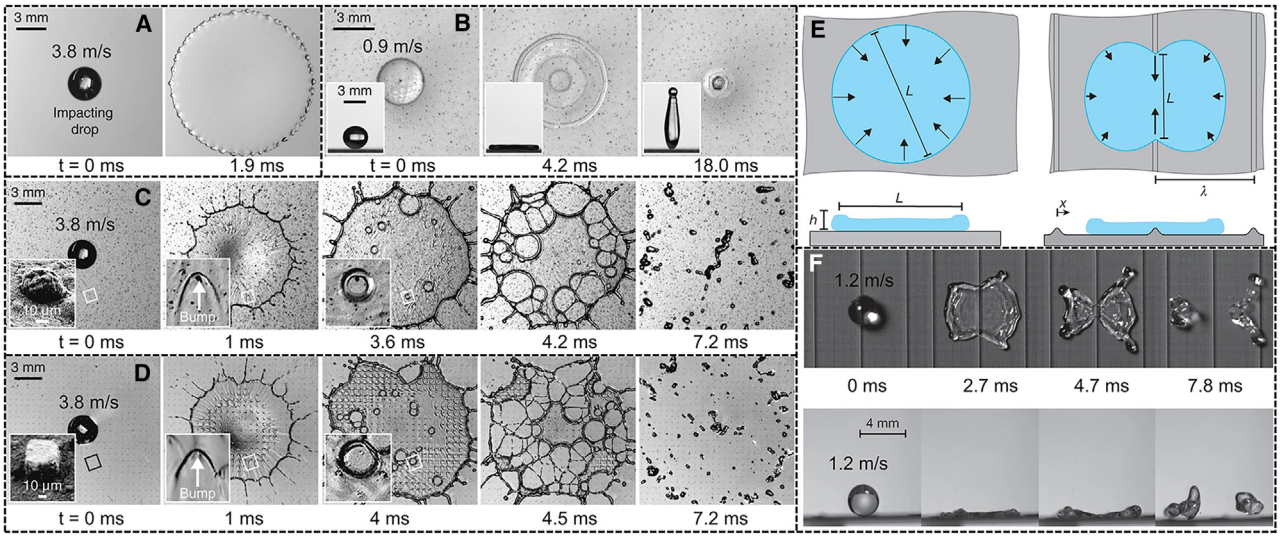

Figure 6. Impact of droplet scattering on contact time

(A) Drop impact on a smooth glass for high-impact velocity.

(B and C) Drop impact on a glass coated by hierarchical superhydrophobic structures for low-impact velocity (B) and for high-impact velocity (C).

(D) Similar dynamics were observed on a superhydrophobic surface with regularly spaced microbumps. Produced with permission.[137]

(E) The top and side view diagrams illustrate how the macroscal texture modifies the thickness profile of water droplets.

(F) Top and side views when a drop impacts the surface with the macroscopic structure, it moves rapidly along the ridge as it recoils. Produced with permission[90] from *Nature*.

velocity data, the contact time between the sliding droplet and the surface can be recalculated. For instance, if the contact angle of the droplets is 151.3°,[139] and assuming a circular contact region, the diameter of the contact region would be 1.3 mm for a sliding droplet with a volume of 10 μL. The contact time of the sliding droplet reaches its maximum when the droplet begins to slide, after which it decreases dramatically. For such a droplet, an initial speed of 0.4 m/s (faster than most raindrops, as shown in Figure 4B) ensures that the contacting time remains below 4 ms, which is nearly the minimum contacting time for a bouncing droplet. Assuming the diameter of the circular contact region area is comparable to the raindrop diameter shown in Figure 4B (the approximate maximum size of a raindrop on a superhydrophobic surface) and that the raindrop maintains its falling speed on the surface (i.e., its velocity is treated as the initial speed). The calculated contact time of raindrops, is shown in Figure 7G. The results show that for both stratiform and convective rain, the contact time is shorter than 2.1 ms, significantly less than 4 ms. Freezing rain droplets retain enough kinetic energy to drive them off the surface, even faster than bouncing off.

Maximizing incubation time to delay icing onset

Research consistently shows that superhydrophobic surfaces can delay the icing of sessile droplets, whether supercooled or not, compared to surfaces with relatively lower contact angles. The delay time ranges from hundreds of seconds to several hours.[145–147] Freezing time is influenced by the heat retention of the droplets, the rate of heat transfer, and the nucleation rate (both homogeneous and heterogeneous). The difference between the initial temperature and the nucleation temperature determines heat retention, while heterogeneous nucleation can raise the freezing temperature. The nucleation temperature of water varies widely, typically between 0°C and −40°C, depending on the nucleation conditions and how well the heterogeneous nucleus matches the ice structure. Superhydrophobic surfaces minimize the contact area between droplets and the solid surface. First, the reduced contact area lowers thermal conductance because the thermal conductivity of air is much lower than that of most solids. Secondly, for pure water in particular, the smaller contact area decreases the likelihood of heterogeneous nucleation. However, there is ongoing debate about which factor plays the dominant role. Experimental conditions such as water purity, humidity, supercooling, thermal transfer method, and temperature lead to varying conclusions. Thanh-Binh Nguyen et al. investigated the relationship between the freezing delay of water droplets in a metastable Cassie-Baxter state and their interfacial fraction with the quartz glass.[144] Their results indicate that the interfacial fraction plays a more significant role than pillar height in reducing adhesion strength, and in delaying freezing time, as shown in Figures 8A and 8B. While the authors attributed the extended freezing time of droplets on surfaces with lower interfacial fractions to poor thermal conductance, we argue that the results suggest heterogeneous nucleation plays a much more critical role in delaying icing than thermal conduction, at least in this experiment. Since the thermal conductivity of quartz glass (k) is a thousand times greater than that of air, the effect of air is negligible when the two are connected in parallel. The thermal conductance of quartz glass is determined by both the contact area (A) and the length (L) following the equation $k \approx \frac{A}{L}$[148].

If the thermal conductance were a dominant role in this experiment, increasing the contact area and decreasing length

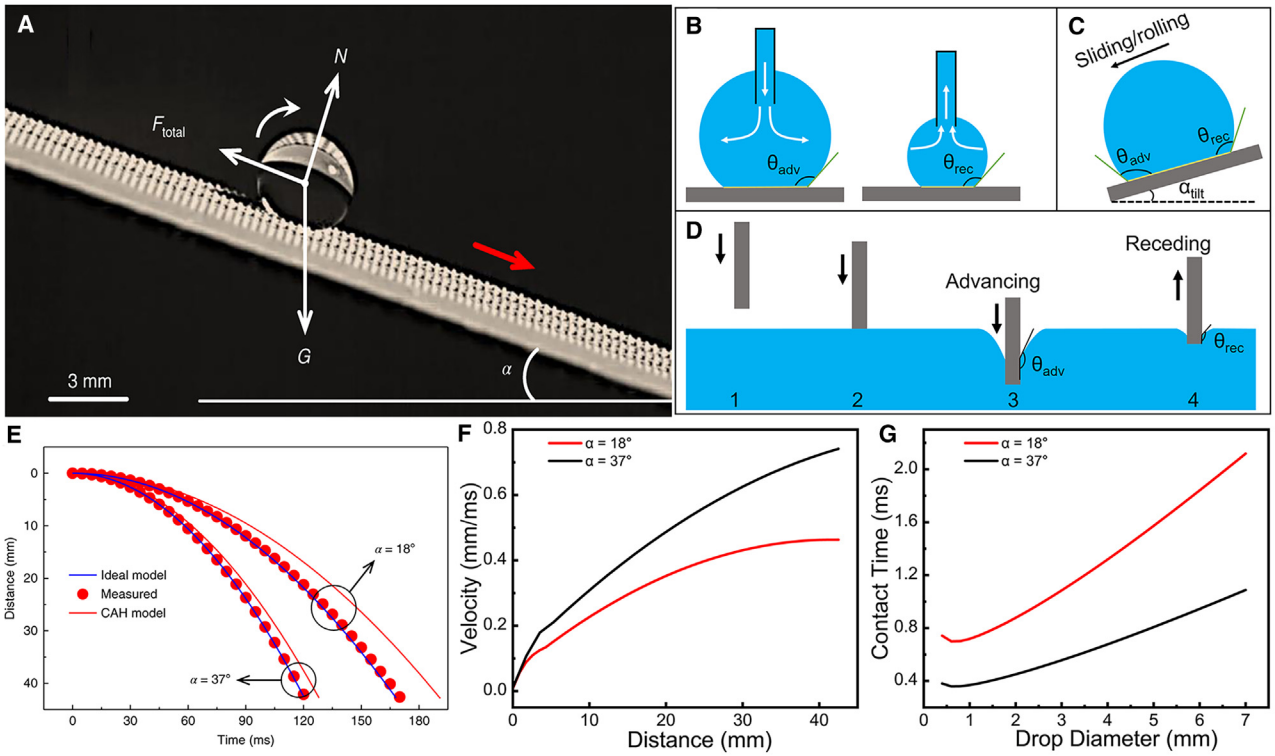

Figure 7. Droplet sliding and surface contact dynamics

(A) Rolling of an n-pentane droplet. N, G, and F_{total} are the normal force, droplet gravity, and drag, respectively.[139]

(B) A schematic of advancing and receding contact angles.

(C) Schematic of dynamic contact angle measurement by using a tilting cradle.

(D) Dynamic contact angle measurement by using Wilhelmy plate method.

(E) The rolling trajectories, for two tilt angles, of the droplet (filled circles) with ideal friction-free rolling (blue line) and the predicted rolling (red line), which is hindered by the CAH.[139] (A) and (E) Produced with permission[139] from *Springer Nature*.

(F) The velocity of the droplet as a function of distance with a slope of 18° and 37°, respectively.

(G) The contact time of the droplet as the function of drop diameter during the rolling off with a slope of 18° and 37°, respectively. The data are analyzed from (E).

would have comparable effects on thermal conductivity. Thus, in Figure 8C, the line would exhibit a slope rather than remain horizontal. However, the heterogeneous nucleation rate is proportional to the contact area and independent of length.[105] Adhesion strength is predominantly determined by the contact area rather than the height of the object. Consequently, increasing the contact area can significantly enhance the adhesion strength between ice and the surface of the object, as demonstrated in Figure 8D. Therefore, more precise experiments are needed to distinguish between these two effects. Heterogeneous nucleation, in particular, often introduces uncertainty in the degree of supercooling, affecting the amount of latent heat released. This further complicates efforts to determine the relative importance of these two factors.

Integration of moisture diffusion path and condensation/frosting position

Fallen water droplets are repelled from superhydrophobic surfaces primarily due to their retained kinetic energy.[149] However, when water molecules condense from vapor onto the surface to form droplets, the net kinetic energy of these molecules approaches zero, as their movement cancels out in different directions. This causes superhydrophobic surfaces to lose their ability to repel water, allowing condensed droplets to remain stable on the surface.[150–152]

As shown in Figure 9A,[153] following condensation, there is a marked reduction in the contact angle of the condensed water droplet, accompanied by a significant expansion in the contact area between the droplet and the superhydrophobic surface. Even when the substrate is tilted at a high angle, gravity cannot dislodge the droplet due to the strong adhesion. Condensation causes a transition from the Cassie–Baxter state to the Wenzel state,[158,159] as the micro air pockets between the droplet and the surface are filled with water. This significantly increases the interface area and consequently, the adhesion strength.[160] As a result, the sliding angle increases sharply, along with the contact angle. Droplets remain attached even when the surface is inverted. Condensed water droplets can adhere to the surface for extended periods, far exceeding the freezing time. This compromises the passive anti-icing ability of surfaces that rely on rapid water droplet expulsion. Therefore, the real challenge for passive anti-icing surfaces arises from humidity rather than freezing rain.[161]

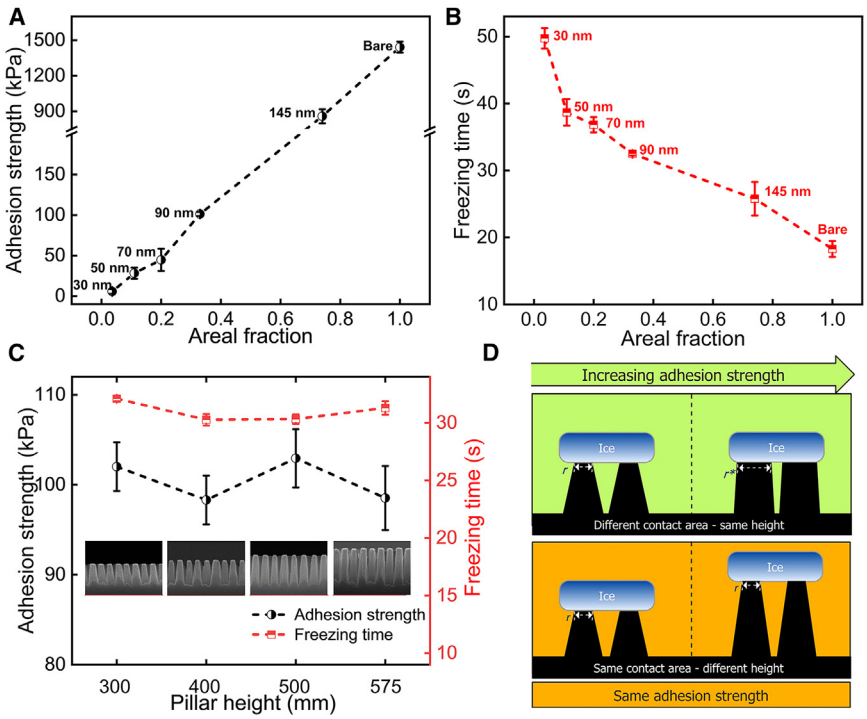

Figure 8. The relationship between freezing delay and areal fraction

(A) Correlation between ice adhesion strength and an areal fraction of the nanostructured surfaces.

(B) Correlation between freezing time and an areal fraction of the nanostructured surface.

(C) Adhesion strength and freezing time value for a given pillar top diameters of 90 nm with samples of different pillar heights (300 nm, 400 nm, 500 nm, and 575 nm).

(D) Schematic of factors contributing to anti-icing performance in terms of actual contact area and nanopillar height. Produced with permission[144] from *Elsevier*.

Superhydrophobic surfaces typically feature complex micro-nanostructures where water vapor tends to condense. Once these areas are covered by condensate, they lose their hydrophobic properties, as shown in Figure 9B,[154] and the surface can no longer repel fallen droplets. If the temperature is low enough, the condensed water will freeze, and this is especially problematic when the water is supercooled. Prolonged condensation in cryogenic environments can cause frost to form indiscriminately across the surface (Figure 9C).[154] In fact, the ice adhesion strength on these surfaces can be higher than on regular surfaces (Figure 9D).[162] When the freezing behavior of superhydrophobic surfaces became a focus of research, it was observed that they could act as viable alternatives to passive anti-icing surfaces. It was discovered that superhydrophobicity is retained when accumulated ice melts into water.[163] As shown in Figure 9E,[156] even partially melted ice slides off the surface along with the water due to gravity, wind, or other forces, as the water flows across the surface. These experiments also revealed that the ice adhesion strength on superhydrophobic surfaces is much lower compared to that on superhydrophilic or hydrophilic surfaces. The authors proposed a potential mechanism, suggesting that frost grows on the peaks of the surface structures, competing with growth in the valleys, as shown in Figure 9F.[157] Vapor transport into the valleys is more difficult, and while frost may nucleate both on the peaks and in the valleys, the growth rate in valleys is much slower. Eventually, frost growth on the peaks restricts vapor transport into the valleys. The size difference between frost on the peaks and in the valleys creates different radii of curvature, with a larger radius on the peaks resulting in lower saturated vapor pressure.[164] As a result, vapor flows from the smaller frost nucleation sites in the valleys to the large frost on peaks, keeping the valley relatively dry as the surface becomes covered in ice.[165] Thus, ice accumulation on such surfaces remains in the Cassie state, characterized by a low interfacial area and a low adhesion strength. These experiments suggest that while icing on the surface may be inevitable, optimizing the location of ice formation can significantly simplify the de-icing process. The key question is identifying the optimal freezing location and ensuring that ice always forms their first.

Residents of high latitudes are accustomed to waking up on winter mornings to find dendritic ice crystals covering their windows. Notably, the spaces between the dendrites remain clean and free of ice. As shown in Figure 10A,[77] this phenomenon is characterized by frozen droplets maintaining a circular dry zone around them, even in areas that were initially wet with condensation. Thermodynamics explains this phenomenon well. As shown in Figure 10B,[144] there is a difference in the saturation pressure of ice and water at temperatures below 0°C, with the largest difference occurring around −15°C. The difference creates a humidity gradient when ice and water coexist nearby, with humidity increasing from ice to water. This gradient generates a thermodynamic force, driven by the Second Law and the tendency for maximum entropy, that pushes water molecules from the high humidity region (water) to the low humidity region (ice). According to Fick's law, the water molecule flux, J, is proportional to diffusion coefficient D and the humidity gradient c: $J = -D\frac{dc}{dx}$[168]. At constant temperature and pressure, there is a fixed distance where J is negligible, represented by δ_{Cr} in Figure 10A. Within this radius, the water flux drain droplets and contributes to ice crystal formation, creating a dry zone between condensation and the growing ice crystals. As the ice crystal grows, the dry zone expands, leaving a significant portion of the surface bare. Thus, under certain conditions, a strategic distribution of ice crystals can suppress condensation and help keep parts of the surface clean. As shown in Figure 10C,[166] a hydrophilic pattern was applied to a superhydrophobic surface. Under cryogenic conditions, condensation first froze on the hydrophilic pattern, and all condensation between ice crystals

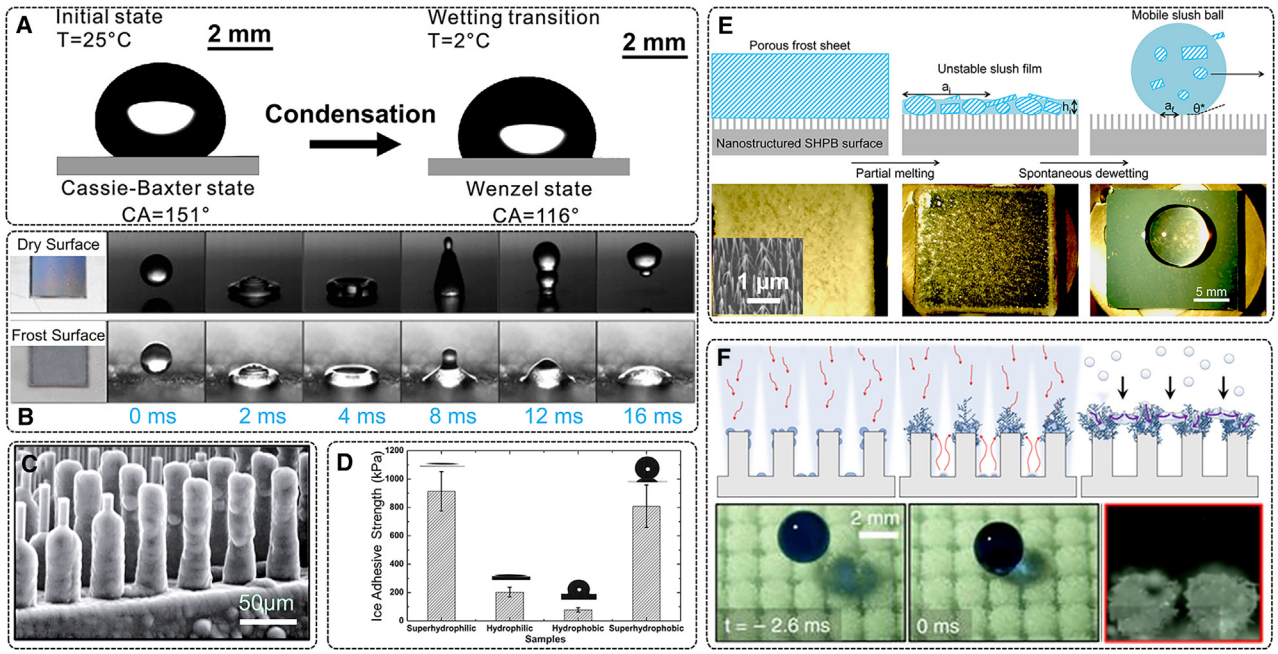

Figure 9. Condensation and frosting on superhydrophobic surfaces

(A) Water droplet transition from Cassie-Baxter state to Wenzel state in the condensation process on a superhydrophobic surface. Produced with permission[153] from the *American Chemical Society.*

(B) Photograph of the dry surface and frosted surface along with sequential high-speed video images of droplet impact.

(C) ESEM images of frost formation on a superhydrophobic surface comprising of an array of hydrophobic square posts. Produced with permission[154] from *AIP publishing.*

(D) The average ice adhesion strength on different films. Produced with permission[155] from *AIP Publishing.*

(E) Schematic of the dynamic defrosting process and Top-down images of dynamic defrosting. Produced with permission[156] from the *American Chemical Society.*

(F) Conceptual overview of our nonsuperhydrophobic technique to trap frost and ice in the Cassie state. Produced with permission[157] from the *American Physical Society.*

dried due to the humidity sink effect of ice.[169] Additionally, frost adhesion strength on these patterned surfaces is relatively low, making the subsequent de-icing process easier. On superhydrophobic surfaces, frost growth transitions from an along-surface mode to an off-surface mode,[167] as shown in Figure 10D. This shift reduces the contact area of ice with the surface, resulting in lower adhesion strength. As a result, de-icing is much easier on superhydrophobic surfaces compared to normal surfaces, as demonstrated by the experiment in Figure 10E.

In addition to ice crystals, frost growth can be suppressed by other materials, particularly hygroscopic ones that have a lower saturation vapor pressure over water. These materials readily absorb water. As shown in Figure 11A,[76] the vapor pressure of common hygroscopic liquids, such as saltwater and various concentrations of aqueous propylene glycol solutions, is lower than that of water and ice at specific temperatures. As a result, hygroscopic antifreeze on a surface can create a region of inhibited condensation around it, due to the humidity sink effect of the hygroscopic materials. By regulating the distribution of hygroscopic droplets, the surface can achieve the largest possible clean area, where it remains free of both frost and antifreeze, as shown in Figure 11B.[76] This strategy is easier to manage than controlling crystal growth in fixed locations, and it is more repeatable, controllable, stable, and mature. However, the durability of this method poses a challenge. As hygroscopic solutions absorb water, the quantity and concentration of the solution eventually reduce their vapor pressure advantage over water, causing the region of inhibited condensation to disappear. Experimental results show that the frost suppression effect lasts for about an hour. To extend this frost inhibition period, a hygroscopic liquid reservoir can be placed beneath a porous hydrophobic surface, as shown in Figure 11C.[170] The presence of hygroscopic liquid within the pores effectively inhibits water vapor condensation and frost formation on the upper surface. With appropriately sized and distributed pores, the surface can remain frost-free at −10°C for up to 120 min. Certain hygroscopic materials, such as nucleoproteins and polyelectrolytes, also act as phase-change materials. When these materials absorb moisture, they undergo a phase change, releasing a large amount of latent heat. This process further enhances the durability of frost inhibition at cryogenic temperatures, as shown in Figure 11D.[171]

Passive de-icing of slippery surfaces

When ice accretion on surfaces is unavoidable, reducing the adhesion strength becomes crucial for easier de-icing. On common surfaces such as aluminum, steel, and glass, ice adhesion strength typically exceeds 500 kPa due to strong interactions between the ice and solid surfaces, such as van der Waals forces,

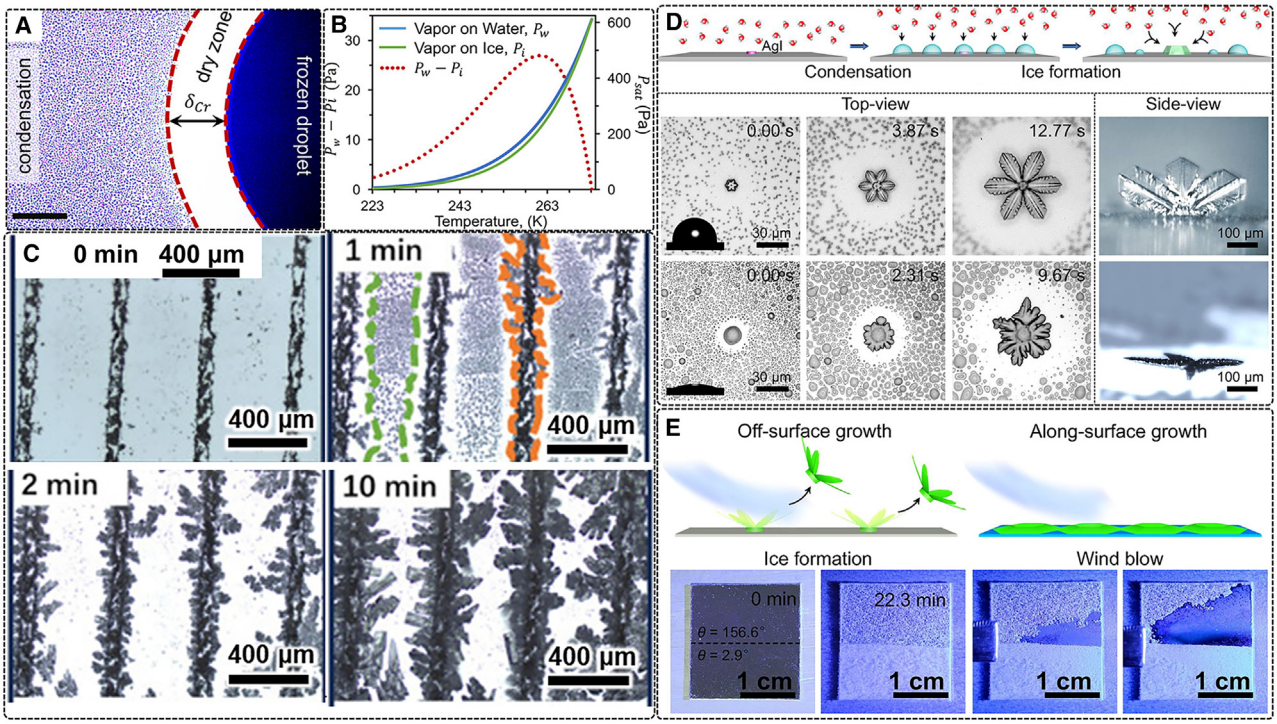

Figure 10. Frost formation on superhydrophobic surfaces with hydrophilic patterns

(A) Frozen water droplet creates a steady-state dry zone between themselves and the surrounding condensation and frost.

(B) Mechanism of the dry zone about ice is its depressed saturation vapor pressure (green curve, right y axis) compared with supercooled water (blue curve, right y axis) at the same temperature.[77] *Copyright © 2018, American Chemical Society.*

(C) Condensation frosting for a duration of 10 min on AgI stipes with pitches of 400 μm. Produced with permission[166] from *Elsevier.*

(D) Distinct ice growth on hydrophobic and hydrophilic surfaces.

(E) A scheme and experiments demonstrating that off-surface growth (OSG) ice can be easily blown away by a breeze, whereas along-surface growth (ASG) ice remains stuck to the solid surface. Reproduced with permission.[167]

electrostatic interactions, and even covalent bonding.[172–175] Superhydrophobic surfaces also struggle with ice adhesion. Although they occasionally result in low adhesion strength,[46,176] mechanical de-icing or thawing typically damages the delicate microstructure responsible for superhydrophobicity, making the passive de-icing capability of these surfaces neither repeatable nor durable.[177,178] Inspired by nepenthes pitcher plants, researchers infused a low-freezing-point lubricant into a textured surface to create an artificial slippery surface, as shown in Figure 12A.[179] The surface energy of both the lubricant and the texture is carefully chosen so that, when another liquid contacts the surface, it maintains the lowest net surface energy. Many immiscible liquids, including water, float on these slippery surfaces. Once frozen, ice adhesion strength is significantly lower compared to other surfaces, as shown in Figure 12B,[180–194] due to the presence of the lubricant. First, the solid texture is coated with the liquid lubricant, creating a smooth interface. Second, the ice is separated from the solid texture by the lubricant, resulting in minimal contact between the ice and the surface. These conditions also hinder the nucleation of supercooled water droplets, delaying the icing process. However, as the ice forms from water, the injected lubricant tends to surround the ice due to the ultrahigh surface energy of ice.[195–197] In some cases, the water is already enclosed by the lubricant.[198,199]

This leads to the lubricant depletion, particularly when ice is removed during the de-icing process. Experiments show that ice adhesion strength on slippery surfaces increases with repeated de-icing cycles due to lubricant depletion, as shown in Figure 12C,[200] although the final adhesion strength remains lower than that on bare surfaces. To counteract this depletion, Xiaoda Sun et al.[201] designed a lubricant-releasing slippery surface inspired by poison dart frogs, as shown in Figure 12D. This surface features an outer porous superhydrophobic layer and an underlying layer infused with antifreeze. Water droplets bounce off the surface, and when frost or ice forms, the antifreeze is released in response. This stimulus-responsive design balances ice adhesion strength with lubricant depletion. The strategy used to reduce adhesion strength on superhydrophobic surfaces is applied here as well, though efforts to minimize lubricant depletion also increase contact between the ice and the solid texture.[202] As a result, slippery surfaces can achieve low ice adhesion (around 30 kPa) even after 50 icing/de-icing cycles with the aid of lubricant injection.[203]

Conclusions and future outlook

In this comprehensive review, we first examined the physical mechanisms of icing. When the temperature drops below a critical value at a specific vapor pressure (e.g., 0 °C at 1 atm), water gains a thermodynamic driving force for phase transition,

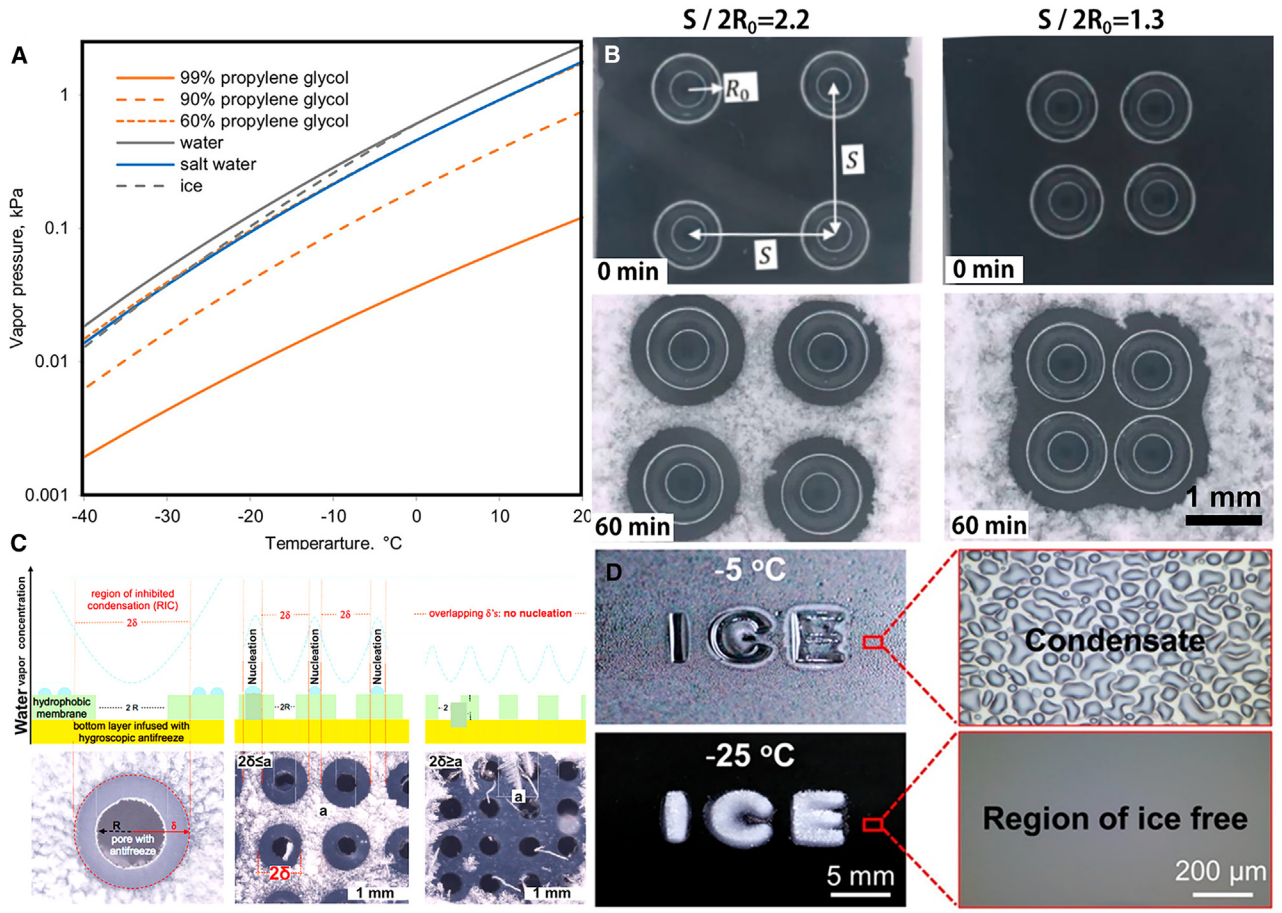

Figure 11. Inhibition of frost growth by hygroscopic materials

(A) Equilibrium water vapor pressure above the surface of water, ice, saturated water salt solution, and 60%, 90%, and 99% by weight propylene glycol water solution in the temperature range of −40°C to 20°C.

(B) Images of condensation frosting around four 2 μL propylene glycol (PG) drops; (a) and (b) Reproduced with permission[76] from the *American Chemical Society*.

(C) Illustration of condensation frosting inhibition on a bilayer coating infused with propylene glycol. Reproduced with permission[170] from the *American Chemical Society*.

(D) Frost-free regions up to 96% on the polyelectrolyte patterns Reproduced with permission[171] from the *American Chemical Society*.

transitioning from a vapor or liquid state to a solid state. To initiate this phase transition, an energy barrier must be overcome by thermal fluctuations, although supercooling can lower this barrier. As a result, predicting the exact timing of the transition, including the temperature and vapor pressure at which it occurs, remains uncertain. This unpredictability makes passive anti-icing strategies based on inhibiting nucleation inconsistent, yielding discrete results. Since freezing is an inevitable thermodynamic process, the goal of passive anti-icing surfaces should not be to prevent freezing entirely. Instead, it is sufficient for these surfaces to prevent ice accretion or accumulation, or to reduce ice adhesion strength if freezing occurs. Therefore, superhydrophobic surfaces, particularly those with rapid water-repelling times, remain promising alternatives for passive anti-icing in specific conditions.

Beyond supercooled water, frost formation is another form of ice accretion that requires attention. Frost lacks the unidirectional kinetic energy of falling droplets, as water molecules condense directly onto the surface. Thus, traditional repelling designs are ineffective against frost. Additionally, frost is hydrophilic, and its accumulation can cause the surface to lose its intended anti-icing properties. Since frost growth is driven by atmospheric humidity, limiting humidity transport to the surface can help inhibit frost formation. Solid or liquid materials with a lower saturated vapor pressure than water can be applied to the surface, creating dry regions that inhibit frost growth. The size and distribution of these dry areas can be controlled by the placement pattern of the added materials. Notably, these materials absorb humidity rather than ice, preventing ice formation around them. However, once they absorb a certain amount of moisture, their ability to inhibit ice growth diminishes. Additionally, special care must be taken to secure these materials to the surface, as they could easily slide off. These materials are typically hydrophilic, so the areas they cover will lose their original wettability and become hydrophilic. At present, slippery surfaces offer the best option for reducing ice adhesion strength, provided the lubricant does not freeze or

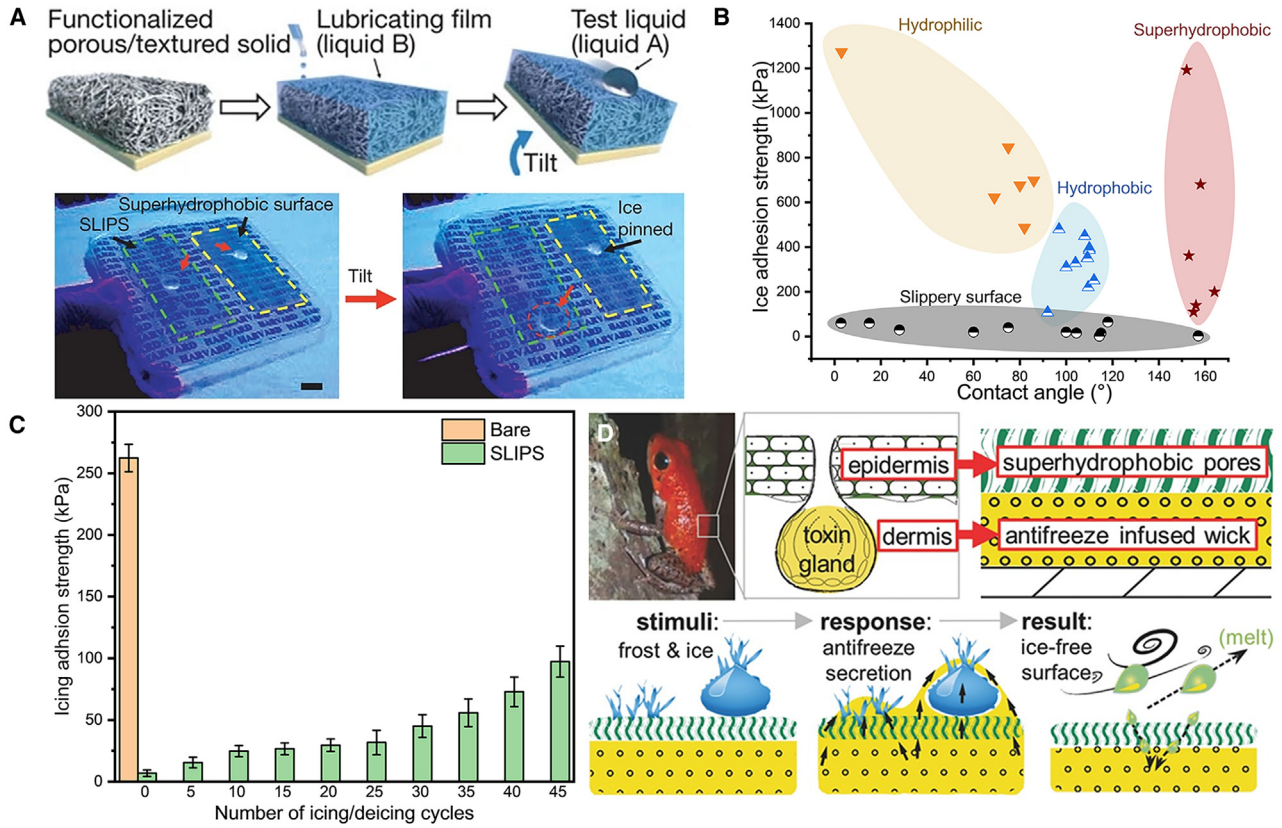

Figure 12. Reducing ice adhesion strength for easier de-icing

(A) Schematics show the fabrication of an SLIPS by the infiltration of a functionalized porous/textured solid with a low-surface energy, chemically inert liquid, and the comparison of ice water mobility on a superhydrophobic surface and SLIPS. Reproduced with permission[179] from *Nature*.

(B) Ice adhesion strength values for different material types. Data is taken from the literature.[180–194]

(C) Evolution of the ice adhesion strength during the icing/deicing cycles. Reproduced with permission[200] from *Wiley*.

(D) Schematic of the stimuli-responsive antifreeze secreting anti-icing coating inspired by the functionality and bilayer architecture of a poison dart frog skin, and the inspired self-responsive substrate design. Reproduced with permission[201] from *Wiley*.

become depleted. The low surface energy of the lubricant is key to the performance of slippery surfaces, though its depletion during de-icing remains a significant challenge.

Despite significant progress in passive anti-icing surfaces over the past few decades, designing a surface capable of performing effectively under all weather conditions remains unrealistic. Currently, the most viable approach is to combine multiple strategies on a single surface to achieve acceptable anti-icing performance under specific conditions. As research continues to advance, emerging smart responsive materials, multilayer composite materials, dynamic surfaces, and nanotechnology are bringing new hope to the field of anti-icing. Nonetheless, several challenges persist, including durability, environmental adaptability, scalability for large-scale applications, and environmental impact. Addressing these challenges necessitates continuous innovation and interdisciplinary collaboration. While there are still hurdles to overcome, the future looks promising. Looking ahead, potential research avenues in the coming years will focus on the development of more efficient, durable, and environmentally friendly anti-icing technologies. This endeavor will involve exploring novel materials with enhanced ice-repellent properties, optimizing surface designs for improved performance across a wider range of conditions, and leveraging advanced manufacturing techniques to ensure scalability and cost-effectiveness. Furthermore, a deeper understanding of the underlying physics and chemistry of ice formation, coupled with advanced computational modeling, will be crucial in guiding the design of next-generation anti-icing surfaces. Ultimately, these efforts will provide robust support for social and economic development, ensuring safer and more reliable infrastructure in icy environments.

ACKNOWLEDGMENTS

This work was supported by the National Key Research and Development Program of China (No. 2018YFA0702304), the Science and Technology Development Key R&D Program of Changchun City (No. 21ZY28), and the Jilin Province Science and Technology Development Project (No. 20180101071JC). We gratefully acknowledge the financial support provided by these programs.

AUTHOR CONTRIBUTIONS

Conceptualization, Z.Z.X. and G.Y.W.; investigation, D.Q.L., S.X.L., and W.T.Z.; writing—original draft, Z.Z.X. and G.Y.W.; writing—review and editing,

Z.Z.X. and G.Y.W.; funding acquisition, G.Y.W.; resources, C.C.Y. and H.S.; supervision, Y.L.

DECLARATION OF INTERESTS

The authors declare no conflict of interest.

REFERENCES

1. Marshall, M. (2020). The Water Paradox and the Origins of Life. Nature *588*, 210–213.
2. Falkenmark, M. (2020). Water Resilience and Human Life Support - Global Outlook for the next Half Century. Int. J. Water Resour. Dev. *36*, 377–396.
3. Bada, J. (2004). How Life Began on Earth : A Status Report. Earth Planet Sci. Lett. *226*, 1–15.
4. Holman, H.P., and Jarrell, T.D. (1923). The Effects of Waterproofing Materials and Outdoor Exposure upon the Tensile Strength of Cotton Yarn. Ind. Eng. Chem. *15*, 236–240.
5. McBurney, D. (1935). Coated Fabrics in Construction Industry. Ind. Eng. Chem. *27*, 1400–1403.
6. Young, T. (1805). An Essay on the Cohesion of Fluids. Phil. Trans. R. Soc., 65–87.
7. Gibbs, J.W. (1878). On the Equilibrium of Heterogeneous Substances. Trans. Conn. Acad. Arts Sci., 343–524.
8. Wenzel, R.N. (1936). Resistance of Solid Surfaces to Wetting by Water. Ind. Eng. Chem. *28*, 988–994.
9. Cassie, A.B.D. (1948). Contact Angles. Discuss. Faraday Soc. *3*, 11–16.
10. Cassie, A.B.D., and Baxter, S. (1944). Wettability of Porous Surfaces. Trans. Faraday Soc. *40*, 546–551.
11. Bormashenko, E., Bormashenko, Y., Stein, T., Whyman, G., and Bormashenko, E. (2007). Why Do Pigeon Feathers Repel Water ? Hydrophobicity of Pennae , Cassie – Baxter Wetting Hypothesis and Cassie – Wenzel Capillarity-Induced Wetting Transition. J. Colloid Interface Sci. *311*, 212–216.
12. Singh, J.K., and Müller-Plathe, F. (2014). On the Characterization of Crystallization and Ice Adhesion on Smooth and Rough Surfaces Using Molecular Dynamics. Appl. Phys. Lett. *104*, 2–7.
13. Zhang, X., Ding, B., Bian, Y., Jiang, D., and Parkin, I.P. (2018). Synthesis of Superhydrophobic Surfaces with Wenzel and Cassie – Baxter State : Experimental Evidence and Theoretical Insight. Nanotechnology *29*, 485601.
14. Erbil, H.Y., and Cansoy, C.E. (2009). Range of Applicability of the Wenzel and Cassie - Baxter Equations for Superhydrophobic Surfaces. Langmuir *25*, 14135–14145.
15. Onda, T., Shibuichi, S., Satoh, N., and Tsujii, K. (1996). Super-Water-Repellent Fractal Surfaces. Langmuir *12*, 2125–2127.
16. Ulman, A. (1996). Formation and Structure of Self-Assembled Monolayers. Chem. Rev. *96*, 1533–1554.
17. Barthlott, W., and Neinhuis, C. (1997). Purity of the Sacred Lotus, or Escape from Contamination in Biological Surfaces. Planta *202*, 1–8.
18. Tuteja, A., Choi, W., Ma, M., Mabry, J.M., Mazzella, S.A., Rutledge, G.C., McKinley, G.H., and Cohen, R.E. (2007). Designing Superoleophobic Surfaces. Science *318*, 1618–1622.
19. Ahuja, a, Taylor, J.A., Lifton, V., Sidorenko, A.A., Salamon, T.R., Lobaton, E.J., Kolodner, P., and Krupenkin, T.N. (2008). A Simple Geometrical Approach to Electrically Tunable Superlyophobic Surfaces. Langmuir *24*, 9–14.
20. Liu, T.L., and Kim, C.J.C.J. (2014). Turning a Surface Superrepellent Even to Completely Wetting Liquids. Science *346*, 1096–1100.
21. Li, C., Chang, G., Wu, S., Yang, T., Zhou, B., Tang, J., Liu, L., Guan, R., Zhang, G., Wang, J., and Yang, Y. (2024). Highly Transparent, Superhydrophobic, and Durable Silica/Resin Self-Cleaning Coatings for Photovoltaic Panels. Colloids Surfaces A Physicochem. Eng. Asp. *693*, 133983.
22. Liu, K., and Jiang, L. (2011). Metallic Surfaces with Special Wettability. Nanoscale *3*, 825–838.
23. Liu, Y., Liu, K., Liu, J., and Hua, J. (2023). Two-Stage Thiol-Ene Click Reaction for Fluorine-Free Superhydrophobic Fabrics with Buoyancy Boost and Drag Reduction. Polym. Test. *129*, 108266.
24. Zhang, H., Cai, S., Zhang, H., Ling, L., Zuo, Y., Tian, H., Meng, T., Xu, G., Bao, X., and Xue, M. (2024). Hydroxyapatite/Palmitic Acid Superhydrophobic Composite Coating on AZ31 Magnesium Alloy with Both Corrosion Resistance and Bacterial Inhibition. Front. Mater. Sci. *18*, 240678.
25. Qiao, A., Huang, R., Penkova, A., Qi, W., He, Z., and Su, R. (2022). Superhydrophobic, Elastic and Anisotropic Cellulose Nanofiber Aerogels for Highly Effective Oil/Water Separation. Sep. Purif. Technol. *295*, 121266.
26. Long, X., Xu, J., Li, C., Liu, J., Qing, Y., and Long, C. (2023). Long-Lived Superhydrophobic Fabric-Based Films via Fenton Reaction for Efficient Oil/Water Separation. Sep. Purif. Technol. *324*, 124523.
27. Sheraz, M., Choi, B., and Kim, J. (2023). Enhancing Textile Water Repellency with Octadecyltrichlorosilane (OTS) and Hollow Silica Nanoparticles. Polymers *15*, 4065.
28. Science, E. (2018). The Impact of Expressway Snowmelt Agent Usage on the Environment in an Extreme Freezing Snow and Sleet Condition The Impact of Expressway Snowmelt Agent Usage on the Environment in an Extreme Freezing Snow and Sleet Condition. IOP Conf. Ser. Earth Environ. Sci. *191*, 012073.
29. Ye, Q. (2014). Building Resilient Power Grids from Integrated Risk Governance Perspective: A Lesson Learned from China's 2008 Ice-Snow Storm Disaster. Eur. Phys. J. Spec. Top. *223*, 2439–2449.
30. Gent, R.W., Dart, N.P., and Cansdale, J.T. (2000). Aircraft Icing. Phil. Trans. R. Soc. A *358*, 2873–2911.
31. Gantasala, S., Tabatabaei, N., Cervantes, M., and Aidanpää, J.O. (2019). Numerical Investigation of the Aeroelastic Behavior of a Wind Turbine with Iced Blades. Energies *12*, 2422–2424.
32. Ryerson, C.C. (2011). Ice Protection of Offshore Platforms. Cold Reg. Sci. Technol. *65*, 97–110.
33. City, N.E.W.Y. (2019). Epic Arctic Mission Will Lock Research Ship in Ice China ' s Tree-Planting Could Falter in a Warming World. Nature *573*, 473–474.
34. Frankenstein, S., and Tuthill, A.M. (2002). Ice Adhesion to Locks and Dams: Past Work; Future Directions? J. Cold Reg. Eng. *16*, 83–96.
35. Seker, D., Karatas, H., and Egrican, N. (2004). Frost Formation on Fin-and-Tube Heat Exchangers. Part I - Modeling of Frost Formation on Fin-and-Tube Heat Exchangers. Int. J. Refrig. *27*, 367–374.
36. Parent, O., and Ilinca, A. (2011). Anti-Icing and de-Icing Techniques for Wind Turbines: Critical Review. Cold Reg. Sci. Technol. *65*, 88–96.
37. Andenæs, E., Jelle, B.P., Ramlo, K., Kolås, T., Selj, J., and Foss, S.E. (2018). The Influence of Snow and Ice Coverage on the Energy Generation from Photovoltaic Solar Cells. Sol. Energy *159*, 318–328.
38. Jiang, X., Wang, Y., Shu, L., Zhang, Z., Hu, Q., and Wang, Q. (2015). Control Scheme of the De-Icing Method by the Transferred Current of Bundled Conductors and Its Key Parameters. IET Gener. Transm. Distrib. *9*, 2198–2205.
39. Juanjuan, W., Chuang, F., Yiping, C., Hong, R., Shukai, X., Tao, Y., and Licheng, L. (2012). Research and Application of DC De – Icing Technology in China Southern Power Grid. IEEE Trans. Power Deliv. *27*, 1234–1242.
40. Zhao, Z., Chen, H., Liu, X., Wang, Z., Zhu, Y., and Zhou, Y. (2020). Novel Sandwich Structural Electric Heating Coating for Anti-Icing/de-Icing on Complex Surfaces. Surf. Coat. Technol. *404*, 126489.

41. Farzaneh, M. (2000). Ice Accretions on High-Voltage Conductors and Insulators and Related Phenomena. Philos. Trans. R. Soc. A Math. Phys. Eng. Sci. *358*, 2971–3005.

42. Laforte, J.L., Allaire, M.A., and Laflamme, J. (1998). State-of-the-Art on Power Line de-Icing. Atmos. Res. *46*, 143–158.

43. Péter, Z., Farzaneh, M., and Kiss, L.I. (2007). Assessment of the Current Intensity for Preventing Ice Accretion on Overhead Conductors. IEEE Trans. Power Deliv. *22*, 565–574.

44. Sanzo, D., and Hecnar, S.J. (2006). Effects of Road De-Icing Salt (NaCl) on Larval Wood Frogs (Rana Sylvatica). Environ. Pollut. *140*, 247–256.

45. Norrström, A.C., and Jacks, G. (1998). Concentration and Fractionation of Heavy Metals in Roadside Soils Receiving De-Icing Salts. Sci. Total Environ. *218*, 161–174.

46. Chen, Z., Song, L., Wang, Y., Tao, H., Liu, Z., Wang, T., Ye, F., He, Y., and Lin, J. (2024). Air Pocket-Optimization Strategy for Micro/Nanostructures Fabricated by Femtosecond Laser Technology for Anti-Icing Performance Improvement. Appl. Surf. Sci. *655*, 159454.

47. Deng, Y., Du, F., Chen, Z., Lv, P., Yin, Z., He, M., Xue, M., and Li, H. (2024). Functionalized Superhydrophobic Coatings with Electro-Photothermal Effect for All-Day Durable Anti-Icing. Adv. Mater. Interfac. *11*, 2300869.

48. Su, J.F., Guo, Y.D., Xie, X.M., Zhang, X.L., Mu, R., Wang, Y.Y., and Tan, Y.Q. (2019). Smart Bituminous Material Combining Anti-Icing and Self-Healing Functions Using Electrothermal Graphene Microcapsules Containing Oily Rejuvenator. Construct. Build. Mater. *224*, 671–681.

49. Jiang, S., Diao, Y., and Yang, H. (2022). Recent Advances of Bio-Inspired Anti-Icing Surfaces. Adv. Colloid Interface Sci. *308*, 102756.

50. Lee, S.H., Kim, J., Seong, M., Kim, S., Jang, H., Park, H.W., and Jeong, H.E. (2022). Magneto-Responsive Photothermal Composite Cilia for Active Anti-Icing and de-Icing. Compos. Sci. Technol. *217*, 109086.

51. Shen, Y., Wu, X., Tao, J., Zhu, C., Lai, Y., and Chen, Z. (2019). Icephobic Materials: Fundamentals, Performance Evaluation, and Applications. Prog. Mater. Sci. *103*, 509–557.

52. Yuan, Y., Wang, L., Liu, G., and Liao, R. (2020). Fabrication of Ultralow Ice-Adhesion Slippery Liquid Infused Porous Surfaces on Aluminum Alloy (7075-T651). Coatings *10*, 1025–1035.

53. Chen, J., Chen, X., Hao, Z., Wu, Z., Selim, M.S., Yu, J., and Huang, Y. (2024). Robust and Superhydrophobic Polydimethylsiloxane/Ni@Ti3C2Tx Nanocomposite Coatings with Assembled Eyelash-Like Microstructure Array: A New Approach for Effective Passive Anti-Icing and Active Photothermal Deicing. ACS Appl. Mater. Interfaces *16*, 26713–26732.

54. Yang, D., Bao, R., Clare, A.T., Choi, K.-S., and Hou, X. (2024). Phase Change Surfaces with Porous Metallic Structures for Long-Term Anti/de-Icing Application. J. Colloid Interface Sci. *660*, 136–146.

55. Vicente, A., Rivero, P.J., Rehfeld, N., Stake, A., García, P., Carreño, F., Mora, J., and Rodríguez, R. (2024). Icephobic Coating Based on Novel SLIPS Made of Infused PTFE Fibers for Aerospace Application. Polymers *16*, 571.

56. Liu, Q., Yang, Y., Huang, M., Zhou, Y., Liu, Y., and Liang, X. (2015). Durability of a Lubricant-Infused Electrospray Silicon Rubber Surface as an Anti-Icing Coating. Appl. Surf. Sci. *346*, 68–76.

57. Qian, C., Zhou, F., Wang, T., Li, Q., Hu, D., Chen, X., and Wang, Z. (2022). Pancake Jumping of Sessile Droplets. Adv. Sci. *9*, 2103834.

58. Pan, W., Wu, S., Huang, L., and Song, J. (2021). Large-Area Fabrication of Superhydrophobic Micro-Conical Pillar Arrays on Various Metallic Substrates. Nanoscale *13*, 14023–14034.

59. Xie, Z., Tian, Y., Shao, Y., Wang, H., Chen, R., Zhu, X., and Liao, Q. (2023). Recent Progress in Anti-Icing and Deicing Applications of the Photothermal Conversion Materials. Prog. Org. Coating *184*, 107834.

60. Cong, Q., Qin, X., Chen, T., Jin, J., Liu, C., and Wang, M. (2023). Research Progress of Superhydrophobic Materials in the Field of Anti-/De-Icing and Their Preparation: A Review. Materials *16*, 5151.

61. Wang, L., Gong, Q., Zhan, S., Jiang, L., and Zheng, Y. (2016). Robust Anti-Icing Performance of a Flexible Superhydrophobic Surface. Adv. Mater. *28*, 7729–7735.

62. Beysens, D. (2006). Dew Nucleation and Growth. Compt. Rendus Phys. *7*, 1082–1100.

63. Zehui, Z., Zelinlan, W., Guang, L., Dengke, C., Kaiteng, Z., Yantong, Z., Jichen, C., Shize, S., Xiaolin, L., and Huawei, C. (2023). Liquid-like Slippery Surface with Passive-Multi Active Strategy Integration for Anti-Icing/de-Icing. Chem. Eng. J. *474*, 145541.

64. Xu, Z., Yin, H., Jiang, Y., Jiang, Z., Liu, Y., Yang, C.C., and Wang, G. (2024). Enhanced Stability and Durability of Cassie-Baxter State in Aluminum-Based Superhydrophobic Surfaces Fabricated via Nanosecond Laser Ablation. J. Mater. Res. Technol. *33*, 7586–7595.

65. Wang, L., Li, D., Jiang, G., Hu, X., Peng, R., Song, Z., Zhang, H., Fan, P., and Zhong, M. (2024). Dual-Energy-Barrier Stable Superhydrophobic Structures for Long Icing Delay. ACS Nano *18*, 12489–12502.

66. Pan, R., Zhang, H., and Zhong, M. (2021). Triple-Scale Superhydrophobic Surface with Excellent Anti-Icing and Icephobic Performance via Ultrafast Laser Hybrid Fabrication. ACS Appl. Mater. Interfaces *13*, 1743–1753.

67. Xuan, S., Yin, H., Li, G., Zhang, Z., Jiao, Y., Liao, Z., Li, J., Liu, S., Wang, Y., Tang, C., et al. (2023). Trifolium Repens L.-Like Periodic Micronano Structured Superhydrophobic Surface with Ultralow Ice Adhesion for Efficient Anti-Icing/Deicing. ACS Nano *17*, 21749–21760.

68. Yang, P., Yin, K., Song, X., Wang, L., Deng, Q., Pei, J., He, Y., and Arnusch, C.J. (2024). Airflow Triggered Water Film Self-Sculpturing on Femtosecond Laser-Induced Heterogeneously Wetted Micro/Nanostructured Surfaces. Nano Lett. *24*, 3133–3141.

69. Wang, L., Yin, K., Deng, Q., Huang, Q., and Arnusch, C.J. (2024). Multi-scale Hybrid-Structured Femtosecond Laser-Induced Graphene with Outstanding Photo-Electro-Thermal Effects for All-Day Anti-Icing/Deicing. Carbon N. Y. *219*, 118824.

70. He, Y., Yin, K., Wang, L., Wu, T., Chen, Y., and Arnusch, C.J. (2024). Femtosecond Laser Structured Black Superhydrophobic Cork for Efficient Solar-Driven Cleanup of Crude Oil. Appl. Phys. Lett. *124*.

71. Zhang, X., Sun, P., Yan, T., Huang, Y., Ma, Z., Zou, B., Zheng, W., Zhou, J., Gong, Y., and Sun, C.Q. (2015). Water's Phase Diagram: From the Notion of Thermodynamics to Hydrogen-Bond Cooperativity. Prog. Solid State Chem. *43*, 71–81.

72. Moelwyn-Hughes, E.A., and Lewis, D. (1960). Physical Chemistry, *107*.

73. Myers, T.G., Charpin, J.P.F., and Thompson, C.P. (2002). Slowly Accreting Ice Due to Supercooled Water Impacting on Acold Surface. Phys. Fluids *14*, 240–256.

74. Azimi Dijvejin, Z., Jain, M.C., Kozak, R., Zarifi, M.H., and Golovin, K. (2022). Smart Low Interfacial Toughness Coatings for On-Demand de-Icing without Melting. Nat. Commun. *13*, 5119.

75. Ahmadi, S.F., Spohn, C.A., Nath, S., and Boreyko, J.B. (2020). Suppressing Condensation Frosting Using an Out-of-Plane Dry Zone. Langmuir *36*, 15603–15609.

76. Sun, X., Damle, V.G., Uppal, A., Linder, R., Chandrashekar, S., Mohan, A.R., and Rykaczewski, K. (2015). Inhibition of Condensation Frosting by Arrays of Hygroscopic Antifreeze Drops. Langmuir *31*, 13743–13752.

77. Ahmadi, S.F., Nath, S., Iliff, G.J., Srijanto, B.R., Collier, C.P., Yue, P., and Boreyko, J.B. (2018). Passive Antifrosting Surfaces Using Microscopic Ice Patterns. ACS Appl. Mater. Interfaces *10*, 32874–32884.

78. Schlitter, J. (2018). The Second Law of Thermodynamics as a Force Law. Entropy *20*, 234.

79. Jellinek, H. (1967). Liquid-like (Transition) Layer on Ice. J. Colloid Interface Sci. *25*, 192–205.

80. Wu, Y., Kang, J., and Liu, F. (2008). Pressure Induced Wurtzite-to-Zinc Blende Phase Transition in ZnO at Finite Temperature. J. Mater. Res. *23*, 3347–3352.

81. Matsumoto, A. (2000). Thermodynamic Functions at Isobaric Process of van Der Waals Gases. Zeitschrift für. Naturforschung A *55*, 851–855.

82. Matsumoto, A. (2021). The First-Order Phase Transition of Melting for Molecular Crystals by Frost-Kalkwarf Vapor- A Nd Sublimation-Pressure Equations. Zeitschrift für. Naturforschung A *76*, 1159–1164.

83. Elsner, A. (2015). Thermodynamic Equilibrium of the Saturated Fluid with a Free Surface Area and the Internal Energy as a Function of the Phase-Specific Volumes and Vapor Pressure. Engineering *07*, 577–596.

84. Rachmayani, A.N. (1964). Thermal Equilibrium of the Atmosphere with a Convective Adjustment. J. Atmos. Sci. *21*, 361–385.

85. Graeber, G., Schutzius, T.M., Eghlidi, H., and Poulikakos, D. (2017). Spontaneous Self-Dislodging of Freezing Water Droplets and the Role of Wettability. Proc. Natl. Acad. Sci. USA *114*, 11040–11045.

86. Fischer, L.J., Von Arx, S., Wechsler, U., Züst, S., and Worlitschek, J. (2016). Phase Change Dispersion, Potentially a New Class of Heat Transfer Fluids. J. Phys, Conf. Ser. *745*, 032133.

87. Macklin, W.C., and Payne, G.S. (1967). A Theoretical Study of the Ice Accretion Process. Q. J. R. Meteorol. Soc. *93*, 195–213.

88. Yao, X., Hawkins, S.C., and Falzon, B.G. (2018). An Advanced Anti-Icing/de-Icing System Utilizing Highly Aligned Carbon Nanotube Webs. Carbon N. Y. *136*, 130–138.

89. Liu, G.Y., Yuan, Y., Liao, R.J., Xiang, H.Y., Wang, L., Yu, Q., and Zhang, C. (2022). Robust and Self-Healing Superhydrophobic Aluminum Surface with Excellent Anti-Icing Performance. Surface. Interfac. *28*, 101588.

90. Bird, J.C., Dhiman, R., Kwon, H.M., and Varanasi, K.K. (2013). Reducing the Contact Time of a Bouncing Drop. Nature *503*, 385–388.

91. Yamamoto, R., Kowalski, D., Zhu, R., Wada, K., Sato, Y., Kitano, S., Zhu, C., Aoki, Y., and Habazaki, H. (2021). Applied Surface Science Fabrication of Superhydrophobic Copper Metal Nanowire Surfaces with High Thermal Conductivity. Appl. Surf. Sci. *537*, 147854.

92. Jia, C., Zhu, J., and Zhang, L. (2022). Study on Preparation of Superhydrophobic Copper Surface by Milling and Its Protective Performance. Materials *15*, 1939–1944.

93. Zhang, R., Hao, P., Zhang, X., and He, F. (2018). Supercooled Water Droplet Impact on Superhydrophobic Surfaces with Various Roughness and Temperature. Int. J. Heat Mass Tran. *122*, 395–402.

94. Chaudhary, G., and Li, R. (2014). Freezing of Water Droplets on Solid Surfaces: An Experimental and Numerical Study. Exp. Therm. Fluid Sci. *57*, 86–93.

95. Aliotta, F., Giaquinta, P.V., Ponterio, R.C., Prestipino, S., Saija, F., Salvato, G., and Vasi, C. (2014). Supercooled Water Escaping from Metastability. Sci. Rep. *4*, 7230–7235.

96. Kostinski, A., and Cantrell, W. (2007). Entropic Aspects of Supercooled Droplet Freezing. J. Atmos. Sci. *65*, 2961–2971.

97. Knopf, D.A., and Alpert, P.A. (2023). Atmospheric Ice Nucleation. Nat. Rev. Phys. *5*, 203–217.

98. Schutzius, T.M., Jung, S., Maitra, T., Eberle, P., Antonini, C., Stamatopoulos, C., and Poulikakos, D. (2015). Physics of Icing and Rational Design of Surfaces with Extraordinary Icephobicity. Langmuir *31*, 4807–4821.

99. Reinhardt, A., and Doye, J.P.K. (2012). Free Energy Landscapes for Homogeneous Nucleation of Ice for a Monatomic Water Model. J. Chem. Phys. *136*, 054501.

100. Fletcher, N.H. (2009). The Chemical Physics of Ice (Cambridge University Press).

101. Li, K., Xu, S., Shi, W., He, M., Li, H., Li, S., Zhou, X., Wang, J., and Song, Y. (2012). Investigating the Effects of Solid Surfaces on Ice Nucleation. Langmuir *28*, 10749–10754.

102. Li, C., Gao, X., and Li, Z. (2017). Roles of Surface Energy and Temperature in Heterogeneous Ice Nucleation. J. Phys. Chem. C *121*, 11552–11559.

103. Srivastava, S., Terai, Y., Liu, J., Capellini, G., and Xie, Y.H. (2023). Controlling the Nucleation and Growth of Salt from Bodily Fluid for Enhanced Biosensing Applications. Biosensors *13*, 1016–1030.

104. Murray, B.J., O'sullivan, D., Atkinson, J.D., and Webb, M.E. (2012). Ice Nucleation by Particles Immersed in Supercooled Cloud Droplets. Chem. Soc. Rev. *41*, 6519–6554.

105. Zhang, Z., and Liu, X.Y. (2018). Control of Ice Nucleation: Freezing and Antifreeze Strategies. Chem. Soc. Rev. *47*, 7116–7139.

106. Vlasov, V.A. (2019). Activated Complex Theory of Nucleation. Eur. Phys. J. E *42*, 36–38.

107. Binder, K. (2014). Simulations Clarify When Supercooled Water Freezes into Glassy Structures. Proc. Natl. Acad. Sci. USA *111*, 9374–9375.

108. Ji, J., Wang, Y., Zhang, X., Chen, Y., Munyalo, J.M., and Liu, S. (2020). Supercooling Characteristics of Mannitol Phase Transition System under Heterogeneous Nucleation. J. Mater. Sci. *55*, 2994–3004.

109. Guo, Q., and Cheng, P. (2020). Effects of Non-Uniform Temperature of the Ice Nucleus on Heterogeneous Ice Nucleation. Int. J. Heat Mass Tran. *163*, 120404.

110. Bahadur, V., Mishchenko, L., Hatton, B., Taylor, J.A., Aizenberg, J., and Krupenkin, T. (2011). Predictive Model for Ice Formation on Superhydrophobic Surfaces. Langmuir *27*, 14143–14150.

111. Hu, Z., Chu, F., and Wu, X. (2022). Design Principle of Ridge-Textured Superhydrophobic Surfaces for Inducing Pancake Bouncing. Int. Commun. Heat Mass Tran. *136*, 106167.

112. Mehrizi, A.A., Sun, L., Zhang, J., Pang, B., Zhang, K., and Chen, L. (2024). Droplet Impact Dynamics on a Flexible Superhydrophobic Cantilever Wire Mesh. Surface. Interfac. *44*, 103736.

113. Mossop, S.C. (1955). The Freezing of Supercooled Water. Proc. Phys. Soc. B *68*, 193–208.

114. Yaghoubi, M., Ahmadi, N.P., and Yazdani, S. (2024). Fabrication of Robust Superhydrophobic Zinc-Coated Steel with Anti-Corrosion and Self-Cleaning Behavior through a Simple Nickel Galvanic Replacement Reaction. Colloids Surfaces A Physicochem. Eng. Asp. *686*, 133341.

115. Chen, Q., Shen, X., Zhang, Z., and Xu, Q. (2024). Robust Superhydrophobic SiO2/GPE/MWCNTs Durable Composite Coating with Photothermal and Electrothermal Effect for Passive Anti-Icing/Active de-Icing. Prog. Org. Coating *191*, 108438.

116. Mishchenko, L., Hatton, B., Bahadur, V., Taylor, J.A., Krupenkin, T., and Aizenberg, J. (2010). Design of Ice-Free Nanostructured Surfaces Based on Repulsion of Impacting Water Droplets. ACS Nano *4*, 7699–7707.

117. Shu, Y., Chu, F., Hu, Z., Gao, J., Wu, X., Dong, Z., and Feng, Y. (2022). Superhydrophobic Strategy for Nature-Inspired Rotating Microfliers: Enhancing Spreading, Reducing Contact Time, and Weakening Impact Force of Raindrops. ACS Appl. Mater. Interfaces *14*, 57340–57349.

118. Chen, L., Xiao, Z., Chan, P.C., Lee, Y.K., and Li, Z. (2011). A Comparative Study of Droplet Impact Dynamics on a Dual-Scaled Superhydrophobic Surface and Lotus Leaf. Appl. Surf. Sci. *257*, 8857–8863.

119. Boinovich, L., Emelyanenko, A.M., Korolev, V.V., and Pashinin, A.S. (2014). Effect of Wettability on Sessile Drop Freezing: When Superhydrophobicity Stimulates an Extreme Freezing Delay. Langmuir *30*, 1659–1668.

120. Hao, P., Lv, C., and Zhang, X. (2014). Freezing of Sessile Water Droplets on Surfaces with Various Roughness and Wettability. Appl. Phys. Lett. *104*, 161609.

121. Tsenova, B., Mitzeva, R., and Saunders, C. (2009). A Modelling Study of the Effect of Ice Particle Sizes and Relative Velocity on Ice Crystal/Graupel Collisional Charge Transfer. Atmos. Res. *91*, 250–258.

122. Shang, Y., Moze, M., Aksoy, Y.T., Castagne, S., Seveno, D., Golobic, I., and Vetrano, M.R. (2024). Effect of Surface Wettability on Dynamic Behaviors and Freezing Mechanisms of Water Droplets Impacting Cold Surfaces. Phys. Fluids *36*, 092004.

123. Li, H., and Zhang, K. (2019). Dynamic Behavior of Water Droplets Impacting on the Superhydrophobic Surface: Both Experimental Study and Molecular Dynamics Simulation Study. Appl. Surf. Sci. *498*, 143793.

124. Jung, S., Tiwari, M.K., Doan, N.V., and Poulikakos, D. (2012). Mechanism of Supercooled Droplet Freezing on Surfaces. Nat. Commun. *3*, 615–622.

125. Niu, S., Jia, X., Sang, J., Liu, X., Lu, C., and Liu, Y. (2010). Distributions of Raindrop Sizes and Fall Velocities in a Semiarid Plateau Climate: Convective versus Stratiform Rains. J. Appl. Meteorol. Climatol. *49*, 632–645.

126. Liu, Y., Moevius, L., Xu, X., Qian, T., Yeomans, J.M., and Wang, Z. (2014). Pancake Bouncing on Superhydrophobic Surfaces. Nat. Phys. *10*, 515–519.

127. Xiang, H., Yuan, Y., Dai, X., Zhu, T., Zhao, Y., Song, L., and Liao, R. (2024). A Novel Superhydrophobic Al Conductor with Excellent Anti-Icing Performance and Its Mechanism. Surface. Interfac. *46*, 104138.

128. Wu, H., Jiang, K., Xu, Z., Yu, S., Peng, X., Zhang, Z., Bai, H., Liu, A., and Chai, G. (2019). Theoretical and Experimental Studies on the Controllable Pancake Bouncing Behavior of Droplets. Langmuir *35*, 17000–17008.

129. Guo, C., Zhao, D., Sun, Y., Wang, M., and Liu, Y. (2018). Droplet Impact on Anisotropic Superhydrophobic Surfaces. Langmuir *34*, 3533–3540.

130. Song, J., Gao, M., Zhao, C., Lu, Y., Huang, L., Liu, X., Carmalt, C.J., Deng, X., and Parkin, I.P. (2017). Large-Area Fabrication of Droplet Pancake Bouncing Surface and Control of Bouncing State. ACS Nano *11*, 9259–9267.

131. Richard, D., Clanet, C., and Quéré, D. (2002). Contact Time of a Bouncing Drop. Nature *417*, 811.

132. Qian, C., Li, Q., and Chen, X. (2020). Droplet Impact on the Cold Elastic Superhydrophobic Membrane with Low Ice Adhesion. Coatings *10*, 964–974.

133. Weisensee, P.B., Tian, J., Miljkovic, N., and King, W.P. (2016). Water Droplet Impact on Elastic Superhydrophobic Surfaces. Sci. Rep. *6*, 30328.

134. Banitabaei, S.A., and Amirfazli, A. (2017). Droplet Impact onto a Solid Sphere: Effect of Wettability and Impact Velocity. Phys. Fluids *29*, 062111.

135. Mitra, S., Sathe, M.J., Doroodchi, E., Utikar, R., Shah, M.K., Pareek, V., Joshi, J.B., and Evans, G.M. (2013). Droplet Impact Dynamics on a Spherical Particle. Chem. Eng. Sci. *100*, 105–119.

136. Chen, S., and Bertola, V. (2017). Drop Impact on Spherical Soft Surfaces. Phys. Fluids *29*, 082106.

137. Kim, S., Wu, Z., Esmaili, E., Dombroskie, J.J., and Jung, S. (2020). How a Raindrop Gets Shattered on Biological Surfaces. Proc. Natl. Acad. Sci. USA *117*, 13901–13907.

138. Song, D., Song, B., Hu, H., Du, X., and Zhou, F. (2015). Selectively Splitting a Droplet Using Superhydrophobic Stripes on Hydrophilic Surfaces. Phys. Chem. Chem. Phys. *17*, 13800–13803.

139. Pan, S., Guo, R., Björnmalm, M., Richardson, J.J., Li, L., Peng, C., Bertleff-Zieschang, N., Xu, W., Jiang, J., and Caruso, F. (2018). Coatings Super-Repellent to Ultralow Surface Tension Liquids. Nat. Mater. *17*, 1040–1047.

140. Lian, Z., Xu, J., Ren, W., Wang, Z., and Yu, H. (2019). Bouncing Dynamics of Impact Droplets on the Biomimetic Plane and Convex Superhydrophobic Surfaces with Dual-Level and Three-Level Structures. Nanomaterials *9*, 1524–1538.

141. Symon, S., Clanet, C., and Que, D. (2015). Water Impacting on Superhydrophobic Macrotextures. Nat. Commun. *6*, 2–7.

142. Ueda, Y., Yokoyama, S., Nomura, M., Tsujino, R., and Iguchi, M. (2010). Bouncing Behaviors of Suspension Liquid Drops on a Superhydrophobic Surface. J. Vis. *13*, 281–283.

143. Backholm, M., Molpeceres, D., Vuckovac, M., Nurmi, H., Hokkanen, M.J., Jokinen, V., Timonen, J.V.I., and Ras, R.H.A. (2020). Water Droplet Friction and Rolling Dynamics on Superhydrophobic Surfaces. Commun. Mater. *1*, 64–68.

144. Nguyen, T.B., Park, S., and Lim, H. (2018). Effects of Morphology Parameters on Anti-Icing Performance in Superhydrophobic Surfaces. Appl. Surf. Sci. *435*, 585–591.

145. Liu, Y., Fu, K., Liu, J., Tian, Y., Zhang, H., Wang, R., Zhang, B., Zhang, H., Zhou, F., and Zhang, Q. (2019). Design and Preparation of a Multi-Fluorination Organic Superhydrophobic Coating with High Mechanical Robustness and Icing Delay Ability. Appl. Surf. Sci. *497*, 143663.

146. Guo, C., Zhang, M., and Hu, J. (2021). Icing Delay of Sessile Water Droplets on Superhydrophobic Titanium Alloy Surfaces. Colloids Surfaces A Physicochem. Eng. Asp. *621*, 126587.

147. Xie, Z., Wang, H., Geng, Y., Li, M., Deng, Q., Tian, Y., Chen, R., Zhu, X., and Liao, Q. (2021). Carbon-Based Photothermal Superhydrophobic Materials with Hierarchical Structure Enhances the Anti-Icing and Photothermal Deicing Properties. ACS Appl. Mater. Interfaces *13*, 48308–48321.

148. Kleiber, M. (1972). Body Size, Conductance for Animal Heat Flow and Newton's Law of Cooling. J. Theor. Biol. *37*, 139–150.

149. Schutzius, T.M., Jung, S., Maitra, T., Graeber, G., Köhme, M., and Poulikakos, D. (2015). Spontaneous Droplet Trampolining on Rigid Superhydrophobic Surfaces. Nature *527*, 82–85.

150. Parin, R., Martucci, A., Sturaro, M., Bortolin, S., Bersani, M., Carraro, F., and Del Col, D. (2018). Surface & Coatings Technology Nano-Structured Aluminum Surfaces for Dropwise Condensation. Surf. Coat. Technol. *348*, 1–12.

151. Sharma, C.S., Combe, J., Giger, M., Emmerich, T., and Poulikakos, D. (2017). Growth Rates and Spontaneous Navigation of Condensate Droplets Through Randomly Structured Textures. ACS Nano *11*, 1673–1682.

152. Zhao, G., Zou, G., Wang, W., Geng, R., Yan, X., He, Z., Liu, L., Zhou, X., Lv, J., and Wang, J. (2020). Competing E Ff Ects between Condensation and Self-Removal of Water Droplets Determine Antifrosting Performance of Superhydrophobic Surfaces. ACS Appl. Mater. Interfaces *12*, 7805–7814.

153. Cui, J., Wang, T., and Che, Z. (2024). Freezing-Melting Mediated Dewetting Transition for Droplets on Superhydrophobic Surfaces with Condensation. Langmuir *40*, 14685–14696.

154. Varanasi, K.K., Deng, T., Smith, J.D., Hsu, M., and Bhate, N. (2010). Frost Formation and Ice Adhesion on Superhydrophobic Surfaces. Appl. Phys. Lett. *97*, 234102.

155. Chen, J., Liu, J., He, M., Li, K., Cui, D., Zhang, Q., Zeng, X., Zhang, Y., Wang, J., and Song, Y. (2012). Superhydrophobic Surfaces Cannot Reduce Ice Adhesion. Appl. Phys. Lett. *101*, 111603.

156. Boreyko, J.B., Srijanto, B.R., Nguyen, T.D., Vega, C., Fuentes-Cabrera, M., and Collier, C.P. (2013). Dynamic Defrosting on Nanostructured Superhydrophobic Surfaces. Langmuir *29*, 9516–9524.

157. Park, H., Ahmadi, S.F., and Boreyko, J.B. (2021). Using Frost to Promote Cassie Ice on Hydrophilic Pillars. Phys. Rev. Lett. *127*, 044501.

158. Park, K.C., Kim, P., Grinthal, A., He, N., Fox, D., Weaver, J.C., and Aizenberg, J. (2016). Condensation on Slippery Asymmetric Bumps. Nature *531*, 78–82.

159. Cheng, Y.-T., and Rodak, D.E. (2005). Is the Lotus Leaf Superhydrophobic? Appl. Phys. Lett. *86*, 144101.

160. Papadopoulos, P., Mammen, L., Deng, X., Vollmer, D., and Butt, H.-J. (2013). How Superhydrophobicity Breaks Down. Proc. Natl. Acad. Sci. USA *110*, 3254–3258.

161. Raiyan, A., Mohammadian, B., and Sojoudi, H. (2021). Droplet Dynamics and Freezing Delay on Nanoporous Microstructured Surfaces at Condensing Environment. Coatings *11*, 617.

162. Chen, J., Liu, J., He, M., Li, K., Cui, D., Zhang, Q., Zeng, X., Zhang, Y., and Wang, J. (2012). Superhydrophobic Surfaces Cannot Reduce Ice Adhesion Superhydrophobic Surfaces Cannot Reduce Ice Adhesion. Appl. Phys. Lett. *101*, 2012–2015.

163. Zhang, B.X., He, X., Wang, S.L., Zheng, S.F., Yang, Y.R., Wang, X.D., and Lee, D.J. (2022). Explosive Boiling of Argon Nanofilms in the Wenzel or Cassie State on High-Temperature Nanopillar-Arrayed Surfaces. Int. J. Therm. Sci. *172*, 107282.

164. Nath, S., and Boreyko, J.B. (2016). On Localized Vapor Pressure Gradients Governing Condensation and Frost Phenomena. Langmuir *32*, 8350–8365.

165. Zuo, Z., Liao, R., Song, X., Zhao, X., and Yuan, Y. (2018). Improving the Anti-Icing/Frosting Property of a Nanostructured Superhydrophobic Surface by the Optimum Selection of a Surface Modi Fi Er. RSC Adv. *8*, 19906–19916.

166. Tang, J., Okabe, T., Nishimura, K., Sciazko, A., Zhang, H., and Shikazono, N. (2024). International Journal of Heat and Mass Transfer Frost Growth on Silver Iodide (AgI) Stripe Patterned Surface under Condensation Frosting Condition. Int. J. Heat Mass Tran. *235*, 126237.

167. Liu, J., Zhu, C., Liu, K., Jiang, Y., Song, Y., Francisco, J.S., Zeng, X.C., and Wang, J. (2017). Distinct Ice Patterns on Solid Surfaces with Various Wettabilities. Proc. Natl. Acad. Sci. USA *114*, 11285–11290.

168. Atkins, P. (2009). Physical Chemistry, 9th ed. (W.H.Freeman).

169. Boreyko, J.B., Hansen, R.R., Murphy, K.R., Nath, S., Retterer, S.T., and Collier, C.P. (2016). Controlling Condensation and Frost Growth with Chemical Micropatterns. Sci. Rep. *6*, 19131–19145.

170. Sun, X., and Rykaczewski, K. (2017). Suppression of Frost Nucleation Achieved Using the Nanoengineered Integral Humidity Sink Effect. ACS Nano *11*, 906–917.

171. Jin, Y., Wu, C., Yang, Y., Wu, J., He, Z., and Wang, J. (2020). Inhibiting Condensation Freezing on Patterned Polyelectrolyte Coatings. ACS Nano *14*, 5000–5007.

172. Hu, Z., Wu, X., Chu, F., Zhang, X., and Yuan, Z. (2021). Off-Centered Droplet Impact on Single-Ridge Superhydrophobic Surfaces. Exp. Therm. Fluid Sci. *120*, 110245.

173. Alasvand Zarasvand, K., Orchard, D., Clark, C., and Golovin, K. (2022). Effect of Curvature on Durable Ice-Phobic Surfaces Based on Buckling Metallic Plates. Mater. Des. *220*, 110884.

174. Chen, D., Gelenter, M.D., Hong, M., Cohen, R.E., and McKinley, G.H. (2017). Icephobic Surfaces Induced by Interfacial Nonfrozen Water. ACS Appl. Mater. Interfaces *9*, 4202–4214.

175. Wang, Z., Chen, E., and Zhao, Y. (2018). The Effect of Surface Anisotropy on Contact Angles and the Characterization of Elliptical Cap Droplets. Sci. China Technol. Sci. *61*, 309–316.

176. Zhou, L., Tang, J., Kuai, S., Li, Y., Chen, N., Xue, X., and Liu, H. (2024). Facile Fabrication of Robust Superhydrophobic Ice Shedding Coating with Superior Corrosion Resistance and Temperature Durability. ACS Appl. Polym. Mater. *6*, 308–320.

177. Jung, S., Dorrestijn, M., Raps, D., Das, A., Megaridis, C.M., and Poulikakos, D. (2011). Are Superhydrophobic Surfaces Best for Icephobicity? Langmuir *27*, 3059–3066.

178. Huang, X., Sun, M., Shi, X., Shao, J., Jin, M., Liu, W., Zhang, R., Huang, S., and Ye, Y. (2023). Chemical Vapor Deposition of Transparent Superhydrophobic Anti-Icing Coatings with Tailored Polymer Nanoarray Architecture. Chem. Eng. J. *454*, 139981.

179. Wong, T.S., Kang, S.H., Tang, S.K.Y., Smythe, E.J., Hatton, B.D., Grinthal, A., and Aizenberg, J. (2011). Bioinspired Self-Repairing Slippery Surfaces with Pressure-Stable Omniphobicity. Nature *477*, 443–447.

180. Kim, P., Wong, T.S., Alvarenga, J., Kreder, M.J., Adorno-Martinez, W.E., Aizenberg, J., Al, K.I.M.E.T., and Aizenberg, J. (2012). Liquid-Infused Nanostructured Surfaces with Extreme Anti-Ice and Anti-Frost Performance. ACS Nano *6*, 6569–6577.

181. Zhu, L., Xue, J., Wang, Y., Chen, Q., Ding, J., and Wang, Q. (2013). Ice-Phobic Coatings Based on Silicon-Oil-Infused Polydimethylsiloxane. ACS Appl. Mater. Interfaces *5*, 4053–4062.

182. He, Z., Wu, C., Hua, M., Wu, S., Wu, D., Zhu, X., Wang, J., and He, X. (2020). Bioinspired Multifunctional Anti-Icing Hydrogel. Matter *2*, 723–734.

183. Wang, Y., Xue, J., Wang, Q., Chen, Q., and Ding, J. (2013). Verification of Icephobic/Anti-Icing Properties of a Superhydrophobic Surface. ACS Appl. Mater. Interfaces *5*, 3370–3381.

184. Farhadi, S., Farzaneh, M., and Kulinich, S.A. (2011). Applied Surface Science Anti-Icing Performance of Superhydrophobic Surfaces. Appl. Surf. Sci. *257*, 6264–6269.

185. Wang, C., Fuller, T., Zhang, W., and Wynne, K.J. (2014). Thickness Dependence of Ice Removal Stress for a Polydimethylsiloxane Nanocomposite: Sylgard 184. Langmuir *30*, 12819–12826.

186. Song, N., and Benmeddour, A. (2022). Erosion Resistant Hydrophobic Coatings for Passive Ice Protection of Aircraft. Appl. Sci. *12*, 9589–9601.

187. Urata, C., Dunderdale, G.J., England, M.W., and Hozumi, A. (2015). Self-Lubricating Organogels (SLUGs) with Exceptional Syneresis-Induced Anti-Sticking Properties against Viscous Emulsions and Ices. J. Mater. Chem. A *3*, 12626–12630.

188. Wang, Y., Yao, X., Chen, J., He, Z., Liu, J., Li, Q., Wang, J., and Jiang, L. (2015). Organogel as Durable Anti-Icing Coatings. Sci. China Mater. *58*, 559–565.

189. Chen, J., Luo, Z., Fan, Q., Lv, J., and Wang, J. (2014). Anti-Ice Coating Inspired by Ice Skating. Small *10*, 4693–4699.

190. Dou, R., Chen, J., Zhang, Y., Wang, X., Cui, D., Song, Y., Jiang, L., and Wang, J. (2014). Anti-Icing Coating with an Aqueous Lubricating Layer. ACS Appl. Mater. Interfaces *6*, 6998–7003.

191. Chen, J., Dou, R., Cui, D., Zhang, Q., Zhang, Y., Xu, F., Zhou, X., Wang, J., Song, Y., and Jiang, L. (2013). Robust Prototypical Anti-Icing Coatings with a Self-Lubricating Liquid Water Layer between Ice and Substrate. ACS Appl. Mater. Interfaces *5*, 4026–4030.

192. Wang, F., Ding, W., He, J., and Zhang, Z. (2019). Phase Transition Enabled Durable Anti-Icing Surfaces and Its DIY Design. Chem. Eng. J. *360*, 243–249.

193. Liang, B., Zhang, G., Zhong, Z., Huang, Y., and Su, Z. (2019). Superhydrophilic Anti-Icing Coatings Based on Polyzwitterion Brushes. Langmuir *35*, 1294–1301.

194. Sandhu, A., Walker, O.J., Nistal, A., Choy, K.L., and Clancy, A.J. (2019). Perfluoroalkane Wax Infused Gels for Effective, Regenerating, Anti-Icing Surfaces. Chem. Commun. *55*, 3215–3218.

195. Rykaczewski, K., Osborn, W.A., Chinn, J., Walker, M.L., Scott, J.H.J., Jones, W., Hao, C., Yao, S., and Wang, Z. (2012). How Nanorough Is Rough Enough to Make a Surface Superhydrophobic during Water Condensation? Soft Matter *8*, 8786–8794.

196. Rykaczewski, K., Anand, S., Subramanyam, S.B., and Varanasi, K.K. (2013). Mechanism of Frost Formation on Lubricant-Impregnated Surfaces. Langmuir *29*, 5230–5238.

197. Xu, Z., Liu, Y., Yang, C., and Wang, G. (2022). Slippery Lubricant-Infused Porous Surface Based on Porous Aluminum Oxide Used for Anti-Fouling and Passive Defrosting Performance. J. Mater. Sci. *57*, 16665–16674.

198. Hauer, L., Wong, W.S.Y., Donadei, V., Hegner, K.I., Kondic, L., and Vollmer, D. (2021). How Frost Forms and Grows on Lubricated Micro- And Nanostructured Surfaces. ACS Nano *15*, 4658–4668.

199. Sharma, M., Mondal, S.S., Roy, P.K., and Khare, K. (2020). Evaporation Dynamics of Pure and Binary Mixture Drops on Dry and Lubricant Coated Slippery Surfaces. J. Colloid Interface Sci. *569*, 244–253.

200. Yuan, Y., Xiang, H., Liu, G., Wang, L., Liu, H., and Liao, R. (2022). Self-Repairing Performance of Slippery Liquid Infused Porous Surfaces for Durable Anti-Icing. Adv. Mater. Interfac. *9*, 2101968.

201. Sun, X., Damle, V.G., Liu, S., and Rykaczewski, K. (2015). Bioinspired Stimuli-Responsive and Antifreeze-Secreting Anti-Icing Coatings. Adv. Mater. Interfac. *2*, 1400479.

202. Baumli, P., D'Acunzi, M., Hegner, K.I., Naga, A., Wong, W.S.Y., Butt, H.J., and Vollmer, D. (2021). The Challenge of Lubricant-Replenishment on Lubricant-Impregnated Surfaces. Adv. Colloid Interface Sci. *287*, 102329.

203. Nguyen, T.B., Park, S., Jung, Y., and Lim, H. (2019). Effects of Hydrophobicity and Lubricant Characteristics on Anti-Icing Performance of Slippery Lubricant-Infused Porous Surfaces. J. Ind. Eng. Chem. *69*, 99–105.